A TRIDENT SCHOLAR PROJECT REPORT

NO. 455

PIV Flow Field Measurements of Hovering Rotors With Leading-Edge Protuberances

by

Midshipman 1/C Brian P. Cully, USN

UNITED STATES NAVAL ACADEMY
ANNAPOLIS, MARYLAND

USNA-1531-2

REPORT DOCUMENTATION PAGE

Form Approved
OMB No. 0704-0188

1. REPORT DATE *(DD-MM-YYYY)*	**2. REPORT TYPE**	**3. DATES COVERED** *(From - To)*
05-22-17		

4. TITLE AND SUBTITLE
PIV Flow Field Measurements of Hovering Rotors with Leading-Edge Protuberances

5a. CONTRACT NUMBER

5b. GRANT NUMBER

5c. PROGRAM ELEMENT NUMBER

6. AUTHOR(S)
Cully, Brian P.

5d. PROJECT NUMBER

5e. TASK NUMBER

5f. WORK UNIT NUMBER

7. PERFORMING ORGANIZATION NAME(S) AND ADDRESS(ES)

8. PERFORMING ORGANIZATION REPORT NUMBER

9. SPONSORING / MONITORING AGENCY NAME(S) AND ADDRESS(ES)
U.S. Naval Academy
Annapolis, MD 21402

10. SPONSOR/MONITOR'S ACRONYM(S)

11. SPONSOR/MONITOR'S REPORT NUMBER(S)
Trident Scholar Report no. 455 (2017)

12. DISTRIBUTION / AVAILABILITY STATEMENT

This document has been approved for public release; its distribution is UNLIMITED.

13. SUPPLEMENTARY NOTES

14. ABSTRACT

The ability of a helicopter to hover and takeoff/land vertically makes it uniquely suited for many different missions. However, its relatively low forward flight speed has led to a focus on developing helicopters with significantly higher velocity ceilings. The inspiration for the use of protuberances stems from the leading-edge of the pectoral flipper on the humpback whale which, despite its large size, has exceptional maneuverability (i.e., small turning radius) among other whale species.

This project utilized thrust and torque measurements and high-resolution particle image velocimetry (PIV) measurements to analyze performance and wake characteristics of rotors with leading-edge protuberances. Four modified blades, with sinusoidal leading-edges of various amplitudes and wavelengths, were compared to a fifth baseline design. As thrust increased, the modified blades required additional power compared to the baseline; this power increase was directly related to protuberance amplitude, while wavelength had a minimal effect. The baseline and low amplitude blades produced similar flow fields: a concentrated tip vortex and a less turbulent wake sheet. Conversely, the higher amplitude blades produced a significantly more turbulent wake sheet and less coherent tip vortices that dissipated quickly. The higher amplitude blades created more uniform (and more ideal) inflow across the rotor disk, but the generation of vortices along these blades most likely contributed to their greater power requirements.

15. SUBJECT TERMS
PIV, protuberances, rotors, wake, blade twist

16. SECURITY CLASSIFICATION OF:			**17. LIMITATION OF ABSTRACT**	**18. NUMBER OF PAGES**	**19a. NAME OF RESPONSIBLE PERSON**
a. REPORT	**b. ABSTRACT**	**c. THIS PAGE**		78	**19b. TELEPHONE NUMBER** *(include area code)*

U.S.N.A. --- Trident Scholar project report; no. 455 (2017)

PIV FLOW FIELD MEASURMENTS OF HOVERING ROTORS WITH LEADING-EDGE PROTUBERANCES

by

Midshipman 1/C Brian P. Cully
United States Naval Academy
Annapolis, Maryland

_____
(signature)

Certification of Advisers Approval

Assistant Professor Joseph I. Milluzzo
Aerospace Engineering Department

_____
(signature)

_____
(date)

CDR Scott Drayton, USN
Aerospace Engineering Department

_____
(signature)

_____
(date)

Associate Professor David S. Miklosovic
Aerospace Engineering Department

_____
(signature)

_____
(date)

Professor Mark M. Murray
Mechanical Engineering Department

_____
(signature)

_____
(date)

Acceptance for the Trident Scholar Committee

Professor Maria J. Schroeder
Associate Director of Midshipman Research

_____
(signature)

_____
(date)

USNA-1531-2

ABSTRACT

The ability of a helicopter to hover and takeoff/land vertically makes it uniquely suited for many different missions. However, its relatively low forward flight speed has led to a focus on developing helicopters with significantly higher velocity ceilings. A criteria of high-speed helicopters is a rotor system with high efficiency in both hover and forward flight, but traditional design choices (i.e., blade twist) that increase the efficiency of one flight condition often degrade the efficiency of the other. While active systems, such as blade morphing or shape shifting ro- tor blades, have potential to alter loading distribution between flight conditions, these structures can add unwanted weight and complexity to the aircraft. Another solution to achieving twist rate changes could be through the use of passive aerodynamic design: circulation control using leading-edge protuberances.

The inspiration for the use of protuberances stems from the leading-edge of the pectoral flipper on the humpback whale which, despite its large size, has exceptional maneuverability (i.e., small turning radius) among other whale species. Protuberances of various amplitude and wavelength geometries have previously been evaluated on an assortment of lifting surfaces, such as airfoils, wings, helicopter blades, and wind and tidal turbines. Those studies found increases in performance, especially in off-design conditions, most likely due to delayed stall through a mechanism similar to vortex generators. However, there is a dearth of information on how protuberance amplitude and frequency affect the formation and strength of these streamwise vortices, as well as the effect these vortices have on the loading distribution and circulation trailed into the wake.

This project utilized thrust and torque measurements and high-resolution particle image velocimetry (PIV) measurements to analyze performance and wake characteristics of rotors with

leading-edge protuberances. Four modified blades, with sinusoidal leading-edges of various amplitudes and wavelengths, were compared to a fifth baseline design. At lower thrust conditions, the baseline and modified blades had similar power requirements. However, as thrust increased, the modified blades required additional power compared to the baseline; this power increase was directly related to protuberance amplitude, while wavelength had a minimal effect. The baseline and low amplitude blades produced similar flow fields: a concentrated tip vortex and a less turbulent wake sheet. Conversely, the higher amplitude blades produced a significantly more turbulent wake sheet and less coherent tip vortices that dissipated quickly. The higher amplitude blades created more uniform (and more ideal) inflow across the rotor disk, but the generation of vortices along these blades most likely contributed to their greater power requirements.

Keywords: PIV, protuberances, rotors, wake, blade twist

ACKNOWLEDGMENTS

This endeavor could not have been a success without the support of many friends, family, and mentors. First and foremost, I have deep appreciation for the support of my parents, Don and AJ Cully, especially when I was stressed with a difficult problem or upcoming deadline. They helped me maintain a healthier, long-term view of this lengthy research process, and their wise perspectives were invaluable.

Thank you to my primary adviser, Dr. Joseph Milluzzo. Had I known how much would be spent with you on this project (an inestimable amount of hours), I still would have been eager to learn from and work with you.

CDR Scott Drayton challenged me as a student and future naval officer. Long hours in the lab during PIV tests provided ample time to learn from him, and I owe much of my scientific and professional development this year to his mentorship.

My advisers David Miklosovic and Mark Murray offered excellent advice and assistance in my work. Their mentorship, built on many years as experts in their fields, was more than I expected and allowed me to grow considerably as an engineer.

I would also like to thank laboratory technicians Dan Rodgerson and Louise Becnel. They were always available for troubleshooting experiments and provided provided immediate solutions to any problems encountered.

Lastly, I thank the USNA Trident Committee for their time and oversight in this process. The opportunity to undertake a Trident Project has been outstanding and one of the most memorable parts of my Naval Academy experience.

TABLE OF CONTENTS

LIST OF TABLES

LIST OF FIGURES

LIST OF SYMBOLS

A	Blade amplitude, m
A	Disk area, m^2
A_b	Blade area, m^2
c	Blade chord, m
$C_{l_{tip}}$	Lift coefficient at the blade tip
C_Q	Torque coefficient, = $Q/\rho A\Omega^2 R^3$
C_P	Rotor power coefficient, = $P/\rho\pi\Omega^3 R^5$
C_{P_0}	Rotor profile power coefficient, = $P_0/\rho\pi\Omega^3 R^5$
C_{P_i}	Rotor induced power coefficient, = $\kappa C_{P_{ideal}}$
$C_{P_{ideal}}$	Ideal power coefficient, = $C_T^{3/2}/\sqrt{2}$
C_T	Rotor thrust coefficient, = $T/\rho\pi\Omega^2 R^4$
C_P/σ	Power loading coefficient
C_T/σ	Blade loading coefficient
FM	Figure of merit, = $P_{ideal}/P_{measured}$
M	Optical magnification factor
N_b	Number of blades
P	Power, W
Q	Torque, N-m
R	Radius of blade, m

r	Radial distance measured from the hub, m
T	Rotor thrust, N
t/c	Thickness-to-chord ratio
u, v	Velocities in the r- and z-directions, m s^{-1}
v_i	Induced velocity, m s^{-1}
V_{tip}	Rotor tip speed, $= \Omega R$, m s^{-1}
V_{peak}	Peak velocity, m s^{-1}
z	Axial distance measured from the hub plane, m
ζ	Wake age, deg
θ_{TW}	Twist rate, deg
κ	Induced power factor
λ	Inflow ratio, $= v_i/V_{\text{tip}}$
ρ	Flow density, kg m^{-3}
o	Rotor solidity, $= A_b/A$
o_e	Thrust-weighted rotor solidity, $= 3 \int_0^1 \sigma(r) r^2 dr$
Ψ_b	Blade azimuth position, deg
Ω	Rotational speed of the rotor, s^{-1}
ω	Vorticity, s^{-1}

INTRODUCTION

1.1 Background

The ability of a helicopter to hover and takeoff/land vertically makes it uniquely suited for a wide range of missions. However, the helicopter's relatively low forward flight speed has led to efforts to increase its maximum velocity. One criteria of a high-speed helicopter is a rotor system with high hovering efficiency, as well as acceptably high forward flight efficiency. Efficiency is defined as producing the most thrust while minimizing the power required to operate the rotor. The design choices intended to maximize the efficiency of one flight condition, however, often require degrading the efficiency of the other. This investigation examined leading-edge protuberances as a potential means to achieve efficiency increases in both flight regimes.

The inspiration for the use of protuberances stems from the leading-edge of the pectoral flippers on the humpback whale (see Fig. 1.1), which has exceptional maneuverability (i.e., small turning radius) among other whale species despite its large size [1]. The flipper on a whale can be considered analogous to the wing of an aircraft. As such, performance can be measured using similar aerodynamic metrics, such as stall angle, lift-to-drag ratio, and coefficients of lift and drag. Stall occurs when the flow separates over a lifting surface, resulting in reduced lift production and drastically increased drag. Angle of attack is the pitch angle of the model surface measured from the horizontal oncoming airflow; the lift coefficient is a non-dimensionalized representation of lift production; and lift-to-drag ratio is a measure of efficiency. Miklosovic et al. [2] compared a scalloped and baseline flipper-like design and found a 40% increase in stall angle of attack, 6% in-

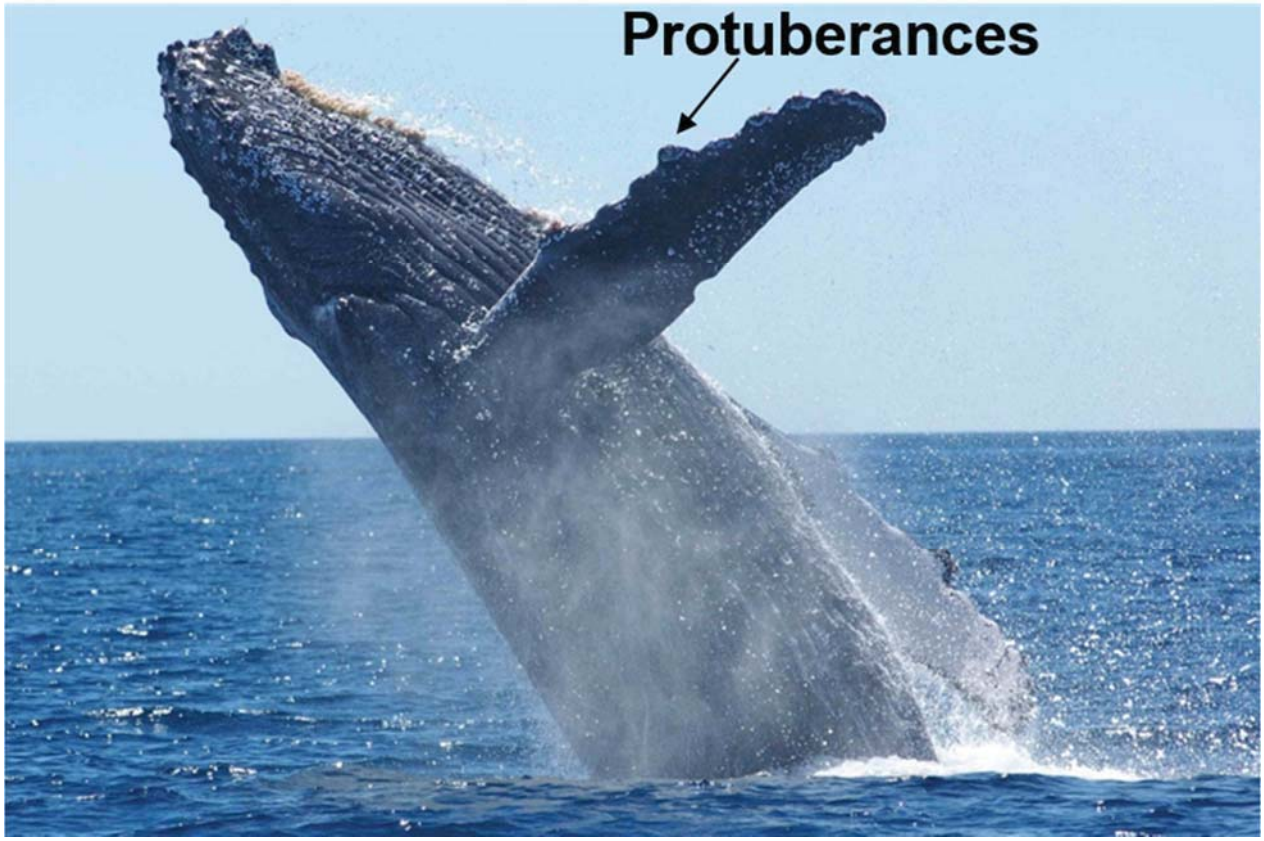

Figure 1.1: Photograph of a humpback whale's pectoral flipper with leading-edge protuberances.

crease in lift coefficient, and an increase in lift-to-drag ratio at pitch angles greater than the baseline flipper's stall point.

Lifting devices are designed for performance and efficiency in specific operating conditions, typically the speed of the oncoming air or water flow. Consquently, performance degrades outside of the design window and, in extreme cases, can stall the lifting device. Scalloped airfoil geometries have also been used to improve efficiency in off-design conditions in applications such as wind turbines and tidal turbine blades (i.e., power production in gusty winds or during slack tides) by mitigating blade stall effects [3–5]. A computational analysis of protuberances on ro- tor blades found that an increase in lift production was achieved within the baseline blade's stall

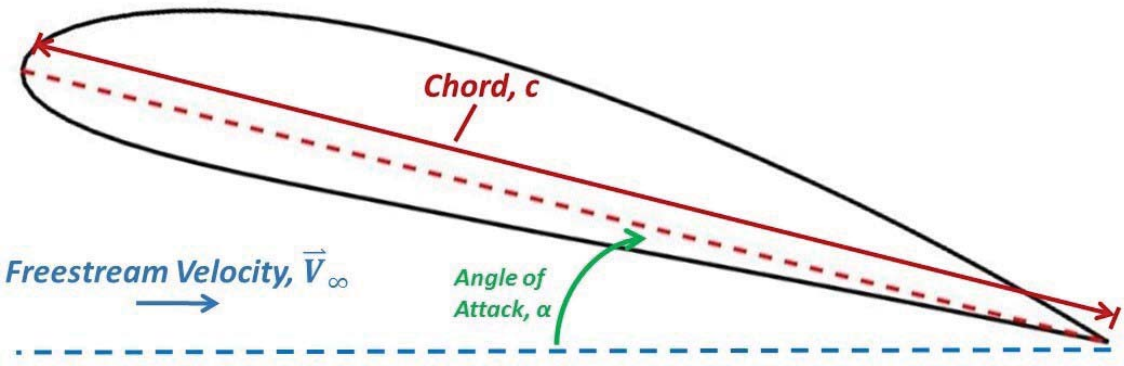

Figure 1.2: Definitions of an airfoil's chord and angle of attack.

region, resulting in an increase in hovering efficiency [6].

1.2 Description of the Problem

Currently, the trade-off between a helicopters's hover efficiency and its forward flight performance is most often encountered in the use of twisted rotor blades. Nose-down blade twist means that the blade is pitched up near the root but flattens near the tip. Pitch is measured by angle of attack, which is the angle between the blade's chord and the horizontal freestream direction; see Fig 1.2. When rotor blades are operating at relatively high pitch angles and lift coefficients (e.g., hover, maneuvering, retreating blade in forward flight, etc.) the utilization of larger amounts of nose-down blade twist produces a more uniform loading distribution along the blade, which significantly reduces the induced power requirements and increases efficiency [7]. Conversely, at lower blade pitch angles and lift coefficients (i.e., advancing blade in high-speed cruise) larger amounts of blade twist can result in degraded performance because of reduced or negative lift production near the blade tip.

Consequently, the design rotor blade twist is often significantly less than that required to maxi-

mize hover efficiency. Thus, there has been considerable interest in altering the blade twist (loading distribution along the blade) between hover and forward flight conditions using shape morphing or ”smart” structures; see Barbarino et al. for a comprehensive review [8]. While the use of smart structures has potential, it increases complexity and adds weight to helicopter. Alternatively, blade twist could be altered using passive aerodynamic design (i.e., circulation control using leading-edge protuberances).

It has been proposed that protuberances improve the post-stall performance of a wing through a mechanism similar to vortex generators. A computational study performed by Pedro and Kobayashi [9] showed the formation of streamwise vortices from the protuberances of an idealized model humpback whale flipper. They found that the protuberances altered the vorticity distribution along the span of the model and increased the downstream vorticity. Experimental work performed by Hansen et al. [10] and Hansen [11] found that the strength of the vortices trailed from the protuberances was directly proportional to the angle of attack of the blade. Mai et al. [12] modeled protuberances using passive vortex generators placed at the airfoil’s leading-edge. They found that the flow stayed attached to higher pitch angles but was only slightly influenced at lower angles. Furthermore, the vortex generators also reduced the magnitude of the nose-down pitching moment associated with dynamic stall.

Protuberances could also be beneficial in delaying the onset of steady and dynamic stall conditions. As a rotor blade rotates in forward flight, the retreating side of the disk travels in the free stream direction and experiences a reduction in local velocity; see Fig 1.3. Consequently, the blades are required to operate at a higher angle of attack to maintain lift. As the aircraft increases its forward velocity, the angles of attack must become exceedingly large, and the blade ultimately stalls. This phenomenon, called retreating blade stall, imposes a ceiling on the maximum flight

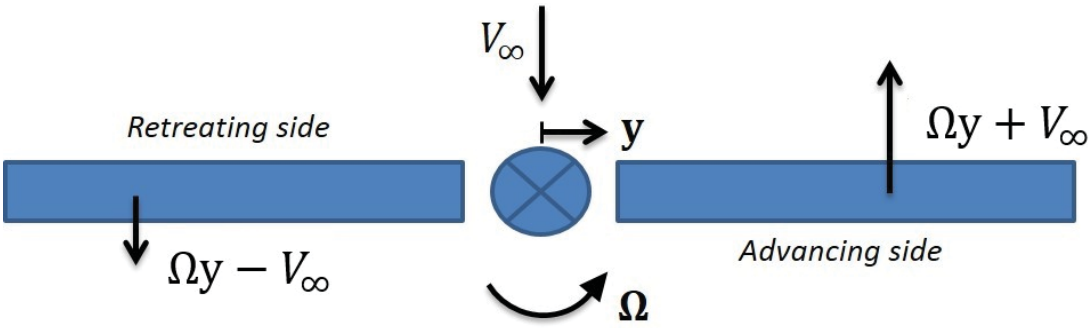

Figure 1.3: Diagram showing the difference in oncoming velocities on each side of the rotor disk in forward flight.

speed of the aircraft. It also poses structural problems as the unsteady airloads produced are an additional source of vibration on the helicopter. The advancing blade operates at lower values of angle of attack but close to its shock-induced flow separation boundary (i.e., the limit at which the speed of sound produces shocks at the blade tip). This time-varying angle of attack, as the rotor blade rotates between advancing and retreating conditions, causes flow separation to occur in a dynamic or time-dependent manner. Therefore, this stall phenonmenon is referred to as dy- namic stall. It is hypothesized that leading-edge protuberances could mitigate these negative effects though vortex generation [13].

While many previous studies have investigated protuberances as a means of delaying the onset of stall [1–6, 9, 10, 10–12, 14–22], few have examined protuberances as a means of circulation control. Moreover, there is a dearth of information on how protuberance amplitude and frequency affect the formation and strength of streamwise vortices, as well as the effect these vortices have on the loading distribution of a rotor system. With this in mind, the goal of the present work is to utilize performance and flow field measurements to gain an initial understanding of protuberances and their relationship to rotor characteristics.

The questions the proposed work seeks to answer are:

1. How does flow structure change as a result of adding protuberances?

2. What are the subsequent effects on rotor performance?

3. How do the amplitude and wavelength of the leading-edge impact these effects?

4. How do vorticity and circulation distributions change?

DESCRIPTION OF EXPERIMENT

The experiment was conducted using a teetering two-bladed rotor system. Five sets of untwisted blades were tested, each with a radius of 0.408 m (16 in), mean chord of 44.45 mm (1.75 in), and NACA 0015 airfoil throughout. This investigation was limited to the simplest case of hovering flight to focus on the transportation of circulation into the wake. Flow field measurements were performed with each rotor configuration operating out of ground effect at a blade loading coefficient of $C_T/\sigma = 0.12$, which was selected to emphasize the effect the protuberances had on the rotor wake (discussed in detail in the Performance Analysis Section). The specific rotor characteristics and test conditions are outlined in Table 2.1.

Table 2.1: Summary of rotor characteristics and test conditions.

Number of Blades, N_b	2
Blade Radius, R	0.408 m (16 in)
Mean Chord, c	44.45 mm (1.75 in)
Thickness to Chord Ratio, t/c	15%
Rotational Frequency, Ω	35 Hz (2,100 RPM)
Blade Loading Coefficient, C_T/σ	0.12
Rotor Tip Speed, V_{tip}	89.1 m s^{-1} (292 ft s^{-1})
Tip Mach Number, M_{tip}	0.27
Tip Reynolds Number, Re_{tip}	280,000

2.1 Blade Design

Performance and flow field measurements were performed on a baseline set of rectangular blades as well as four sets of blades with various sinusoidal leading-edges whose dimensions are defined in Fig. 2.1. Sinusoid amplitude, A, was measured from the mean chord line (i.e., the leading-edge of the baseline blade) to protuberance peak as a percentage of chord length, c. Wave-length, λ, was measured from peak to peak as a percentage of chord length. The amplitudes and wavelengths of the protuberances were selected based on prior experimental work by Johari et al. [14] because they were found to provide a wide range of distinct changes to performance and air flow. Amplitude effects were investigated using three amplitudes (A = 0.025c, 0.05c, and 0.12c) with a constant wavelength λ = 0.50c. Conversely, wavelength effects were examined by varying wavelength (λ = 0.25c and 0.50c) and holding amplitude constant (A = 0.05c). Each blade design is shown in Fig. 2.2. Table 2.2 lists the specific amplitudes and wavelengths examined, as well as the naming conventions used in the current work. Each blade was designed to maintain a constant mean chord length along the entire span of the blade, which yielded a thrust-weighted solidity ($\sigma_e = 3 \int_0^1 \sigma r^2 dr$) of 0.0694 for each blade; an explanation of solidity is discussed in greater detail in the Theory section.

2.2 Performance Measurements

The rotor thrust and torque required were measured as a function of the collective pitch (i.e., a performance sweep) using a combination multi-axis load and torque cell. Tares were obtained by rotating the hub without the rotor blades attached, and these tares were removed from the

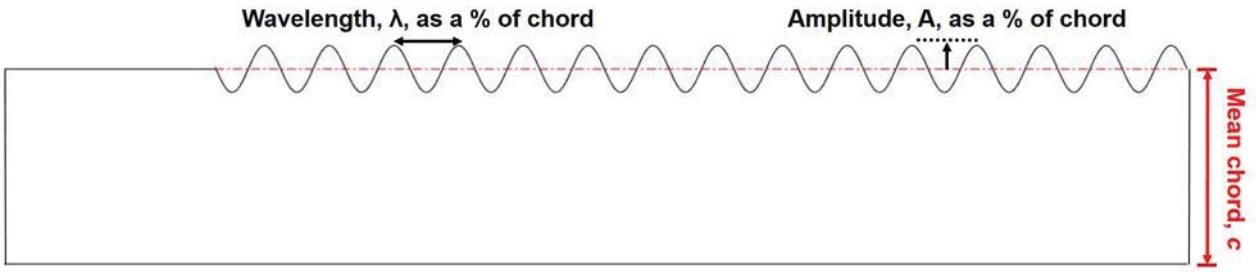

Figure 2.1: Schematic showing protuberance amplitude and wavelength.

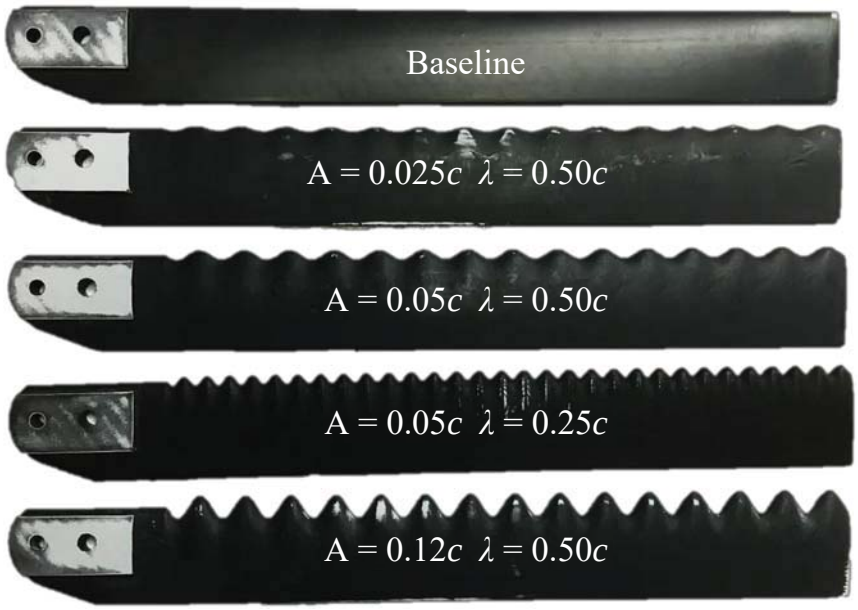

Figure 2.2: Photograph of the blades that were tested.

performance sweeps. Performance sweeps for each blade set were collected for a collective pitch ranging from -2° to 18°. The accuracy of the cell could detect within $C_T/\sigma = \pm 6.3 \times 10^{-5}$ and $C_P/\sigma = \pm 4.0 \times 10^{-6}$ which was sufficient to acquire precise measurements. Rotor performance is based as a measure of rotor power for a given thrust value (a measure of rotor efficiency). In other words, a performance penalty was observed when a rotor blade design requires more power than the baseline design to produce the same thrust output.

2.3 Flow Field Measurements

Flow field measurements were performed using two-component particle image velocimetry (PIV). In order to take the measurements, a laser beam was directed onto a high-intensity rated mirror and reflected through convex and spherical lenses, which diverged the beam into a laser sheet. The sheet intersected the rotor tip path plane. The imaging axis of the camera was aligned orthogonal to the plane of the light sheet and focused on the desired region of interest (ROI). The camera and laser were digitally synchronized such that the laser pulses straddled the camera images. The basic set up of the laser and camera is shown in Fig. 2.3.

2.3.1 Seeding

Neutrally buoyant, submicron tracer particles were seeded into the airflow and illuminated by the laser sheet. These seed particles for the PIV measurements were generated by vaporizing a mineral oil in a high pressure heat exchanger. As the vapor exited the nozzle and mixed with the ambient air it rapidly cooled, condensing into a fog. From a calibration, 95% of seed particles were appoximately 0.22 μm in diameter, which minimizied particle tracking errors in rotor flow

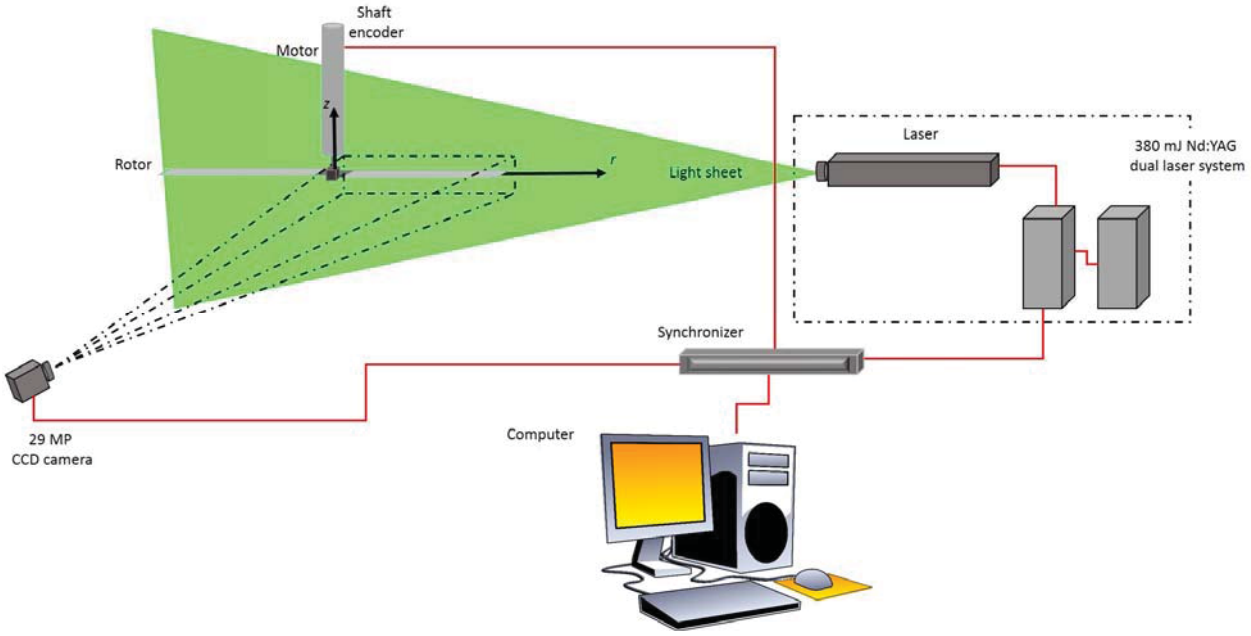

Figure 2.3: Schematic showing the two-bladed rotor and the experimental setup with the laser and camera used for PIV.

fields [23].

2.3.2 Phase-Resolved Flow Measurements

A single 29 mega-pixel CCD camera (6,600-by-4,400 pixel) was used to obtain the flow field measurements. The laser used for the current measurements was an Nd:YAG laser capable of emitting 532 nm light at 380 mJ/pulse when operated at a frequency less than or equal to 10 Hz in frame-straddling mode. Because the rotational frequency of the rotor (35 Hz) exceeded the maximum imaging rate of the camera (1.8 Hz), the imaging system was synchronized with the rotational frequency of the rotor. Therefore, PIV images were only acquired at sub-integer multiples of the rotor frequency (i.e., one image approximately every 35 rotor revolutions).

In PIV, sequential images (forming an image pair) are recorded, separated by a pulse separation

time, dt, which is on the order of microseconds. The images are split into several interrogation areas which have base-2 dimensions (i.e., 64-by-64 or 32-by-32 pixels). In each interrogation area, the mean displacement of all particles within the interrogation area is computed. Using the displacement of the particles and the pulse separation time, the ROI's velocity field can be calculated, with one velocity vector for each interrogation area. The generated velocity field, and the change in velocity fields with respect to phase, can then be used to analyze characteristics of the rotor wake, including the vorticity of spanwise vortices and overall circulation [24] This workflow is diagrammed in Fig. 2.4.

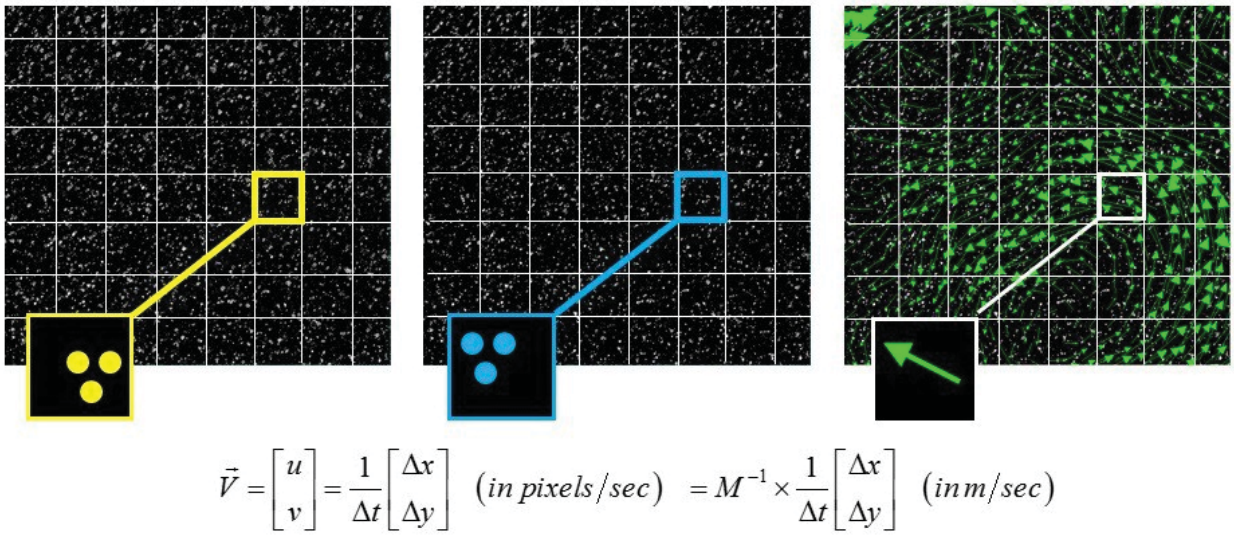

$$\vec{V} = \begin{bmatrix} u \\ v \end{bmatrix} = \frac{1}{\Delta t}\begin{bmatrix} \Delta x \\ \Delta y \end{bmatrix} \ (in\ pixels/sec) \ = M^{-1} \times \frac{1}{\Delta t}\begin{bmatrix} \Delta x \\ \Delta y \end{bmatrix} \ (in\ m/sec)$$

Figure 2.4: Principle of PIV data processing, where M is the optical magnification factor. Here, the particle displacement between the particles' yellow (left) and blue (middle) positions can be resolved into a green (right) velocity vector.

The wake trailed from a rotating wing is most commonly described in terms of the blade phase and the flow wake age; Fig. 2.5 illustrates these terms. Blade azimuth angle, Ψ_b, is the angular position of a rotor blade relative to a reference position. The wake age, ζ, is defined as the time

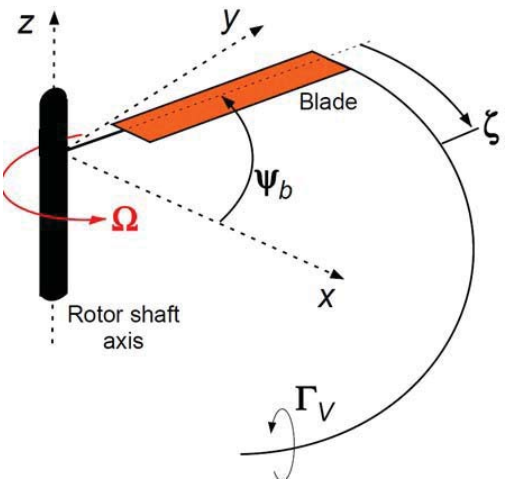

Figure 2.5: Blade position described by wake age.

elapsed since the flow structures were trailed into the wake, expressed in terms of the angular displacement (degrees of rotation) of the corresponding blade. Blade azimuth describes the blade's position, while wake age is used in reference to a vortex or other wake feature. In phase-resolved PIV, images are timed to capture the wake structure of different blade geometries at the same blade azimuth position to compare the flow structures at specific wake ages.

2.3.3 PIV Imaging

Figure 2.6 shows the specific ROI where PIV measurements were conducted. The high-resolution camera was able to resolve the wake in a region encompassing a majority of the blade (approximately 370-by-250 mm, or 0.91-by-0.61R), while maintaining the necessary resolution to resolve the small-scale vortical structures. Two rotor blades (N_b = 2) were mounted to the rotor stand. It was assumed that the rotor system generates the same flow field after each blade pas- sage (with each blade intersecting the light sheet at 3°/N_b). Thus, the wake age necessary to fully resolve the flow for a two-bladed system is 180°. Measurements were taken at blade azimuth in-

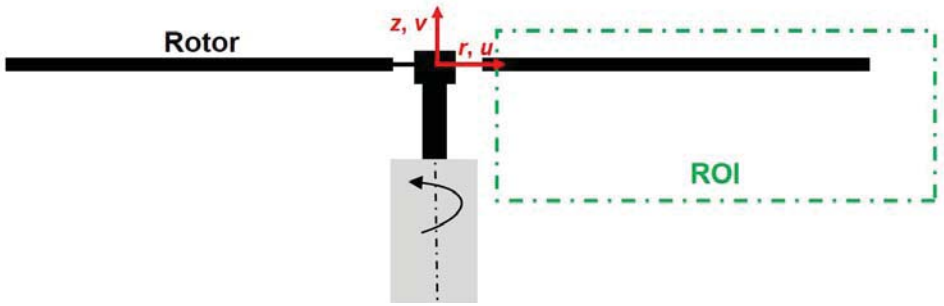

Figure 2.6: Definition of the coordinate system and the region of interest used for flow field measurements.

crements of 30˚ from 0˚ to 180˚, as well as in 3˚ increments at relatively early wake ages (i.e., ≤15˚) to examine the initial formation and development of the wake trailed from the blade. At each blade azimuth position, 300 image pairs were acquired.

2.3.4 Measurement Settings

In order to get accurate data from PIV, proper measurement settings must be used. The first parameter selected was the pulse separation time, dt. A sensitivity study was conducted to identify the optimum dt: particle displacement in an image pair should be greater than the particle's diameter but less than one-fourth the side length of the interrogation area. Additionally, the particles in a vortex follow a curved path, while the displacement in an image pair assumes linear motion; a small pulse separation minimizes curvature effects. This also minimizes acceleration error, which occurs when an accelerating particle in the unsteady flow is assumed to have constant velocity. With these criteria in mind, dt values between 1 and 50 μs were studied, and 18 μs was chosen to optimize the PIV measurements. That is, this value satisfied the above requirements and mini-

mized the amount of spurious vectors compared to other values examined. Finally, the lens's focal length needed to capture a large field of view while maintaining sufficiently large seed particle size on the sensor; a 105 mm lens was used. Furthermore, it was necessary to properly expose each image without subjecting the camera's sensor to too much laser light. An aperture setting of f/8 was sufficient.

2.3.5 Processing Settings

Two sizes of interrogation windows were utilized to extract accurate velocity data from the images. First, a trade study was conducted to identify the settings that most efficiently extract accurate data from the image pairs. Six settings combinations were judged on the quality of processed images of two blade geometries at several wake ages. A recursive processing formula was selected, which conducted four passes through every interrogation area of each image. The first pass used 64-by-64 pixel square interrogation windows that overlapped by 50%. This pass provided an initial guess for the remaining passes to properly identify particle movement. The following three passes used smaller, 32-by-32 pixel interrogation windows that overlapped by 75%. To further improve accuracy in these final passes, an image deformation method was used: the second image's interrogation windows deformed to maximize the number of particles tracked, increasing the fidelity of the velocity measurements. Images were validated through a local median test of the 3-by-3 neighboring vectors, and images with a high number (greater than 5%) of extraneous vectors were ignored. This non-intrusive analysis provided instantaneous velocity fields over global domains [25]. The velocities found were subsequently used to measure vortex strength and achieve a clearer understanding of the mechanism that protuberances employ.

Table 2.2: Summary of the geometry parameters for the baseline and modified blades.

Blade Designation	Amplitude, A	Wavelength, λ
Baseline	0	N/A
A025	0.025c	0.5c
A05	0.05c	0.5c
A05 HF	0.05c	0.25c
A12	0.12c	0.5c

THEORY

3.1 Performance

A rotor's operating conditions can be described by several parameters. The most important properties are the thrust, T, and power, P, produced by the rotor. These values can be non-dimensionalized as coefficients of thrust and power (C_T and C_P, respectively) defined in Eqs. 3.1 and 3.2 below.

$$C_T = \frac{T}{\rho A(\Omega R)^2} \tag{3.1}$$

$$C_P = \frac{P}{\rho A(\Omega R)^3} \tag{3.2}$$

In each equation, A is the rotor disk area (i.e., the area swept out by the rotor blades by the rotation of the rotor), ρ is air density, Ω is the rotor's angular velocity, and R is the rotor's radius. The quantity ΩR is the rotor blade's tip speed, V_{tip}. Because the rotor disk area is not comprised entirely of physical blade surface, the rotor's solidity, σ, is defined in Eq. solidity as the ratio of the rotor blade's physical area to the entire disk area swept by the blade, where r is the local radial position:

$$\sigma = \frac{\text{blade area}}{\text{disk area}} = \frac{A_b}{A} = \frac{N_b c R}{\pi R^2} = \frac{N_b c}{\pi R} \tag{3.3}$$

The blades in this investigation had non-rectangular planform geometries; thus, the local solidity, $\sigma(r)$, varied along the blade span. In order to compare several rotors with different planforms, an equivalent rectangular rotor must be generated to take into account the differences in aerodynamic effects on a varying blade chord. Therefore, thrust-weighted solidity, shown in Eq. 3.4, was

held constant in order to enable this comparison across various geometries.

$$\sigma_e = 3 \int_0^1 \sigma(r) r^2 dr \tag{3.4}$$

$$\sigma_e = 3 \int_0^1 \sigma(r) r^2 dr \tag{3.4}$$

Solidity and the thrust coefficient are used to calculate C_T/σ, the blade loading coefficient, which is blade loading normalized for rotational dynamic pressure. This parameter is related to circulation and must be held constant for flow field measurements.

In order to measure power required by the rotor system, rotor torque is measured. Torque, Q, is then normalized to its coefficient form, C_Q. The torque coefficient is numerically equivalent to the power coefficient.

$$C_Q = \frac{Q}{\rho A \Omega^2 R^3} \tag{3.5}$$

3.2 Fluid Dynamics

The gradient of bound circulation, Γ, along a lifting body are manifested as discrete vortices trailed from the surface. Prandtl's lifting line theory states that vortices are formed as circulation changes along the surface of a wing, with the strength of the vortices equal to the gradient of bound circulation [26]. This theory is diagrammed in Fig. 3.1. Circulation is proportional to lift per- unit-span, L' (see Eq. 3.6); therefore, by producing vortices and altering circulation distribution, protuberances may have the potential to passively modify the loading distribution along a rotor blade in a manner similar to blade twist. Because protuberances have a small effect at low pitch angles (like those encountered by the advancing blade in forward flight) and a large effect at higher pitch angles (like those encountered in hover and by the retreating blade in forward flight) where greater amounts of blade twist are beneficial, leading-edge protuberances would be expected to have the greatest effect on the distribution of bound circulation at natural operating conditions of

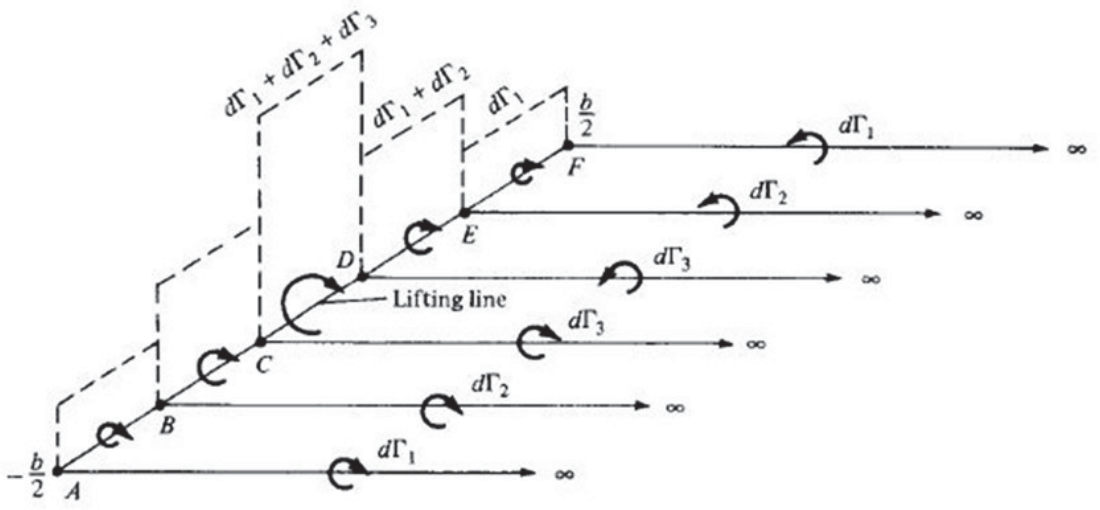

Figure 3.1: The relationship between vortices and circulation [14].

rotor blades.

$$L' = -\rho V \Gamma \tag{3.6}$$

A rotor blade's ideal thrust loading distribution is linear which corresponds to a constant bound circulation over the blade. Ideal circulation, Γ, as a function of radial position, r, is defined in Eqs. 3.7 where $C_{l_{\text{tip}}}$ is the local lift coefficient at the blade tip.

$$\Gamma(r) = \frac{1}{2} cRC_{l_{\text{tip}}} \Gamma = \text{constant} \tag{3.7}$$

Circulation is also related to the blade loading coefficient, C_T/σ, using Eq. 3.8. Blade loading coefficient was held constant in flow field measurements to maintain equal circulation values across blade designs.

$$\Gamma(r) = 2\Omega Rc(C_T/\sigma) \tag{3.8}$$

Blade element momentum theory (BEMT) states that ideal efficiency is achieved with uniform induced velocity through the rotor disk (i.e., requires the least amount of power for a given amount

of thrust produced). In the case of rotor blades, a linear twist along the length of the blade is generally used to recover the losses from low velocities seen near the root. Near the root, local lift coefficients must increase to infinity to account for dynamic pressure reducing to zero. The greater angle of attack (higher lift coefficient) near the root compensates for such losses and maintains lift on this section of the blade. But ideal circulation distribution still degrades as spanwise stall effects occur at higher speeds. Flow field measurements can be used to capture this circulation distribution. It is hypothesized that the strong vortices produced by the protuberances could lead to a more linear curve on an untwisted blade.

3.3 Flow Field Theory

Flow field measurements can be used to obtain the velocity field across an entire region of interest. In each interrogation window, the total velocity magnitude (i.e., the two-dimensional in-plane velocity magnitude induced by the spanwise vortices) will be calculated. The resulting velocity field can be illustrated in instantaneous flow field realizations. Additionally, each image pair can be averaged at each phase to produce phase-averaged total velocity vectors across the flow field. Due to unsteady flow in the wake, the phase-resolved data will not record the tip vortices in the same position for each image. Therefore, when averaging vortical measurements, the wake vortices are collocated, or aligned core-to-core so that the flow characteristics of the vortices are preserved for aperiodic flow. Collocated vortices can be analyzed to produce the flow velocity, $\vec{V}$, at every interrogation window.

A gradient field can be obtained from these raw velocity measurements using the central dif-

ference method, shown below in Eq. 3.9 for the x–component.

$$\frac{dV}{dx} = \frac{V_{i+1} - V_{i-1}}{2\Delta x} \tag{3.9}$$

These gradients are used to find vorticity, ω, or the curl of velocity. This is shown below in Eq. 3.10

$$\omega = \Delta \times \vec{V} = \left(\frac{\partial V_y}{\partial x} - \frac{\partial V_x}{\partial y}\right)\hat{k} \tag{3.10}$$

In this work, only the z-component of vorticity could be calculated due to the planar nature of the 2-D PIV setup. Vorticity can be used to calculate circulation, Γ, which is the total amount of vorticity in a given area (that is, a surface integral of vorticity). Because lift and circulation are directly proportional, calculating circulation along the blade produces the loading distribution across the blade. This will also provide insight into how circulation changes from the addition of protuberances. Flow field measurements will consist of discrete velocity values, however, so circulation will be evaluated using the summation form of the equation instead. Both the integral and summation forms of the relationship are shown below in Eqs. 3.11 and 3.12. Here, Δs is the boundary of the area of interest in the x– or y–direction.

$$\Gamma = -\oint \vec{V} \cdot ds = -\int (\nabla \times \vec{V}) \cdot ds \tag{3.11}$$

$$\Gamma = -\sum_{i=0}^{n} \vec{V}_i \cdot \Delta s = -\sum_{i=0}^{n}\sum_{i=0}^{n} (\nabla \times \vec{V}_i) \cdot \Delta s \tag{3.12}$$

Any flow field can be broken up, or decomposed, into its average and fluctuating constituents. A Reynolds decomposition, shown in Eqn. 3.13, can be used to isolate one component from another (in this case, velocity, u). Here, $\bar{u}$ is the mean velocity of the sample population of measurements, and u' is the turbulent component.

$$u = \bar{u} + u' \tag{3.13}$$

Spanwise vortices will also be used to create swirl velocity profiles, in which the vortex (or co-located average vortex) is cut through the center and the swirl vortices are recorded. Swirl velocity profiles can be used to determine core size and peak swirl velocity, and these values will be examined at each wake age. The swirl velocity profiles can be analyzed to determine how the protuberances affect trailing vortices.

RESULTS

4.1 Performance Analysis

First, performance measurements were analyzed in order to understand how protuberances might change the overall thrust produced and power required by the modified rotor blades compared to the baseline. Figure 4.1 shows the blade loading coefficient, C_T/σ, versus the measured power loading coefficient, C_P/σ, for each rotor configuration operating out of ground effect. At the lower thrust conditions (i.e., $C_T/\sigma \leq 0.06$), the baseline and modified blades had similar power requirements, indicating that at lower collective pitch angles the protuberances had minimal effect on the overall rotor performance. However, as the thrust was increased, the modified blades began to require more power than the baseline blade. The additional power requirements were directly related to the protuberance amplitude. As shown in Fig. 4.1, as the protuberance amplitude was increased, the rotor thrust (blade pitch) at which the power requirements began to rapidly increase occurred at lower thrust conditions. Specifically, the largest amplitude blade required the most power and deviated from baseline performance at the lowest thrust condition (i.e., $C_T/\sigma \approx 0.07$). While protuberance amplitude significantly affected rotor performance, changes in wavelength were found to have a minimal effect (i.e., the A05 and A05 HF blades had similar power requirements at all thrust conditions tested).

The efficiency of each rotor configuration was quantified using the figure of merit ($FM = C_{P_{ideal}}/C_P$), which is plotted versus C_T/σ in Fig. 4.2. Although all blades designs did not reach a peak thrust coefficient, they did achieve a maximum figure of merit. As C_T/σ increased, the

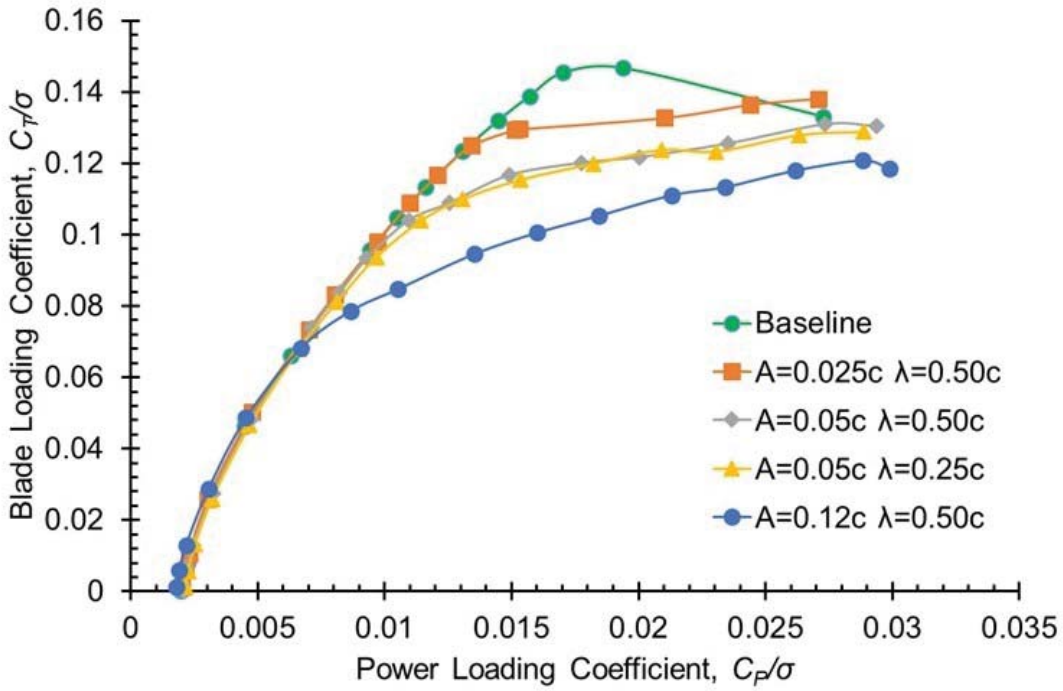

Figure 4.1: Plot of the blade loading coefficient versus measured power loading coefficient for each rotor configuration.

FM reached a peak value before decreasing rapidly. The baseline blade reached a peak FM of approximately 0.6 before the onset of stall drastically increased the power requirements, decreasing the FM; see Fig. 4.2. While each of the modified blades showed a rapid increase in power after a critical thrust condition (causing a significant reduction in the rotor's FM), the rotor thrust continued to increase, suggesting the additional power requirements were not related to the onset of stall; see Fig. 4.1. As previously discussed, increasing protuberance amplitude resulted in the power curves diverging from the baseline at lower thrust conditions. Therefore, the peak FM also decreased with increasing protuberance amplitude, as shown in Table4.1.

The measured power coefficient, C_P versus the ideal power coefficient, $C_{P_{\text{ideal}}}$, for each rotor configuration, is shown in Fig. 4.3. Using modified momentum theory, the total power coefficient

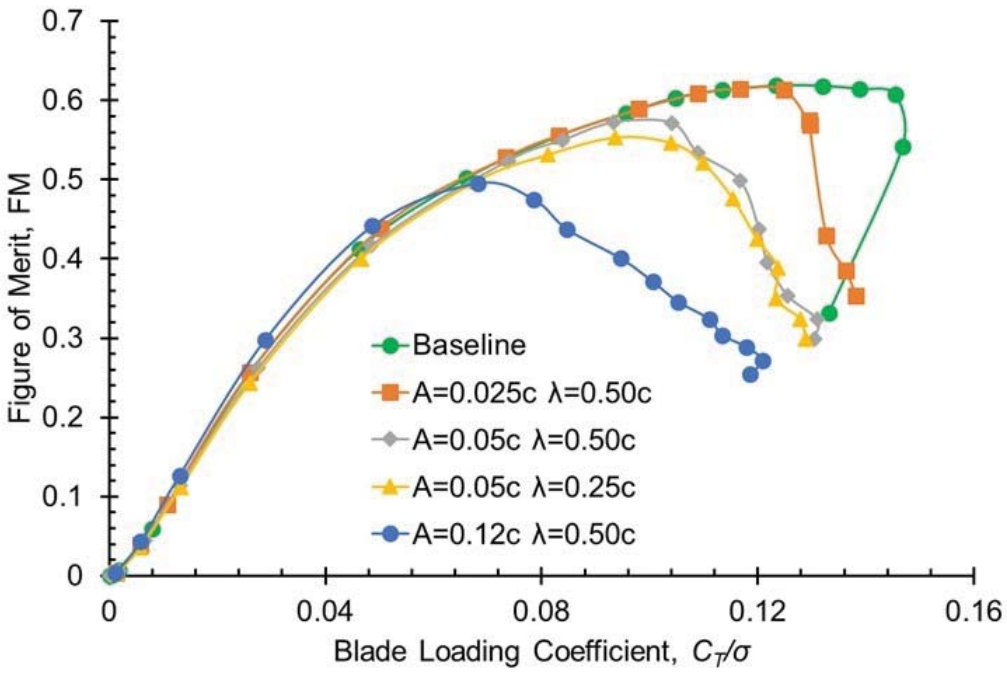

Figure 4.2: Plot of figure of merit versus blade loading coefficient for each rotor configuration.

for a rotor can be approximated as

$$C_P = C_{P_0} + \kappa C_{P_{\text{ideal}}} = C_{P_0} + \kappa \frac{C_T^{3/2}}{2} \tag{4.1}$$

where C_{P_0} is the profile power coefficient, κ is the induced power factor that accounts for many non-ideal effects (e.g., non-uniform inflow, tip losses, non-ideal wake contraction, etc.), and C_T is the rotor thrust coefficient. It is important to note that, in the present work, C_{P_0} was assumed to be independent of rotor thrust, such that the quadratic nature of the airfoil profile drag polar was not modeled [7]. While a slightly better approximation can be obtained by modeling C_{P_0} as a function of rotor thrust, the results from the current work provide a good basis for comparison.

From Eq. 4.1, the slope and y-intercept of the C_P versus $C_{P_{\text{ideal}}}$ curve are κ and C_{P_0}, respectively. Because each blade set was comprised of the same airfoil section (NACA 0015) and equiv-

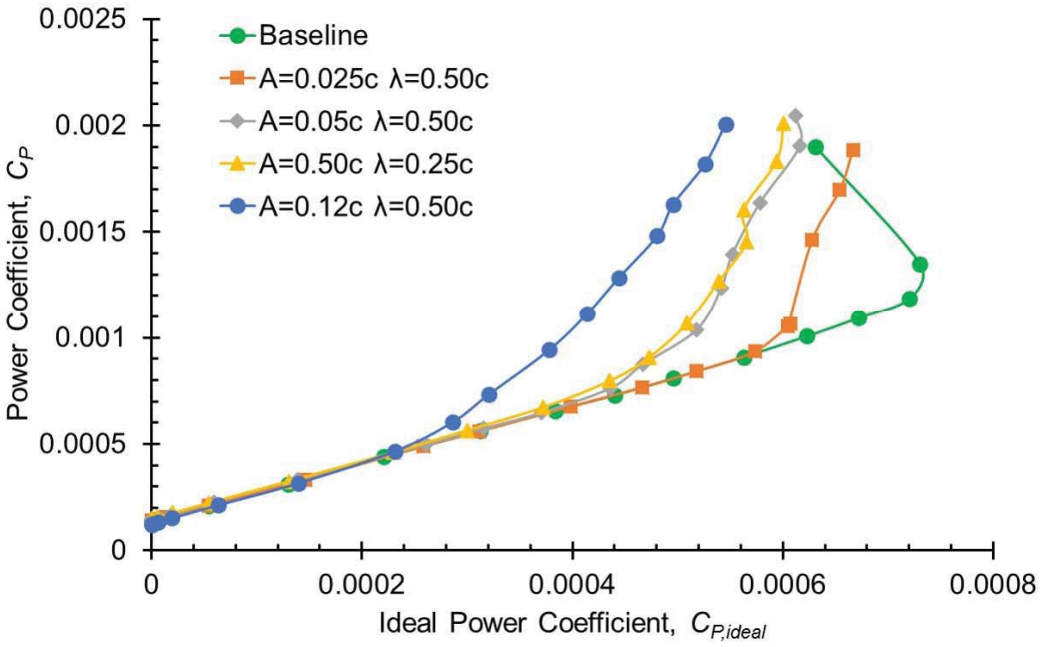

Figure 4.3: Plot of measured power coefficient versus ideal power coefficient for each rotor configuration.

alent thrust weighted solidities (0.0694), they would be expected to incur similar profile power requirements. Figure 4.3 shows that each rotor configuration had similar values for C_{P_0}. Furthermore, for $C_{P_{\text{ideal}}} \leq 0.00024$ (i.e., $C_T/\sigma \leq 0.07$) each configuration also produced equivalent induced power factors, κ. However, as the ideal power (rotor thrust) increased the modified blades began to diverge from the baseline curve.

As previously discussed, the work by Hansen et al. [10] and Hansen [11] found that as airfoil angle of attack was increased the strength of vortices trailed from leading-edge protuberances also increased. Therefore, the additional power requirements of the modified blades could stem from the extra power requirements associated with the creation of vorticity off the protuberances. Because the induced power factor, κ, accounts for non-ideal effects (with the exception of viscosity effects), it was used to quantify the additional power requirements of the modified blades at higher thrust conditions. Table 4.1 shows the induced power factor for each rotor configuration, which was obtained by performing a least-squares fit of Eq. 4.1 to the measured data in Fig. 4.4. As expected, the induced power factor of the modified blades were significantly higher than the baseline's. While the lowest amplitude blade had the largest value of κ, it diverged from the baseline power curve at the highest thrust condition (see Fig. 4.1), resulting in it requiring the least power of the modified blades.

The performance data previously discussed were used to determine the rotor blade loading coefficient, C_T/σ, for subsequent flow field measurements. Because the additional power requirements of the modified blades were believed to be associated with the creation of vorticity by the protuberances, an operating blade loading coefficient was selected such that all but the lowest amplitude blade required more power than the baseline. Therefore, flow field measurements were conducted at a constant blade loading coefficient of $C_T/\sigma = 0.12$.

Table 4.1: Table summarizing the performance characteristics of each rotor configuration.

Blade	Induced power factor, κ	Peak figure of merit, FM_{peak}
Baseline	1.41	0.62
A025	12.9	0.61
A05	9.77	0.57
A05 HF	9.96	0.55
A12	7.09	0.50

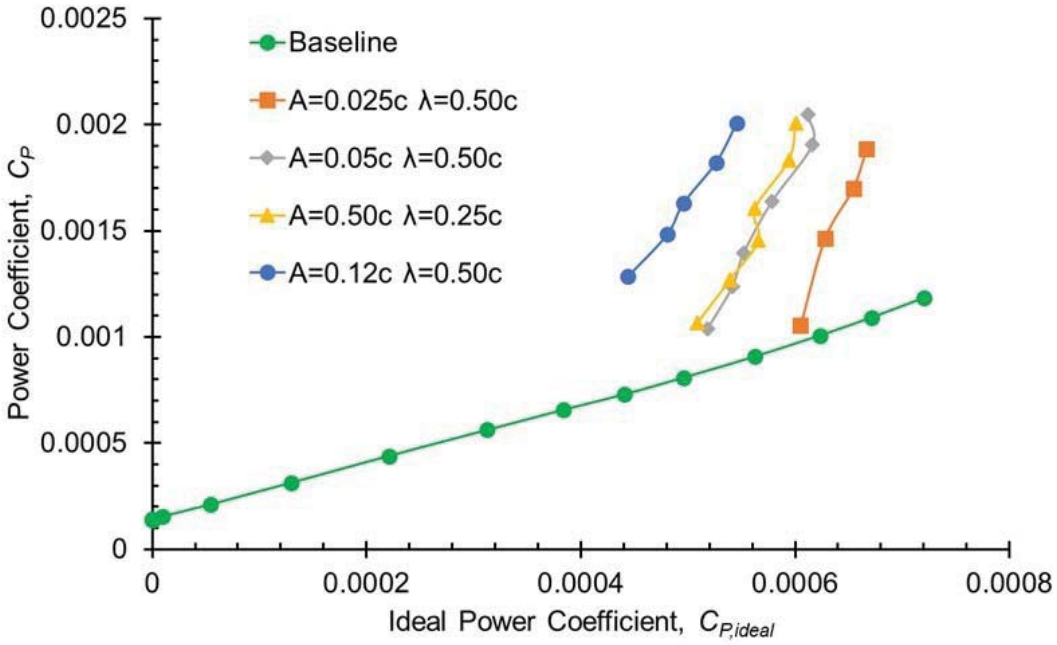

Figure 4.4: Plot of measured power coefficient versus ideal power coefficient used to determine the induced power factor for each rotor configuration.

4.2 Time-Averaged Flow Field Measurements

Time-averaged flow fields were examined to gain an understanding of the overall wake structure produced by each blade. A time-average was obtained by averaging each instantaneous flow field (300 images per azimuth position) at each blade azimuth position, Ψ_b. To prevent biasing the average, only equally-spaced increments were used over the blade azimuth range tested (i.e., $0^\circ \leq \Psi_b \leq 180^\circ$ in 30° increments). Figure 4.5 shows contours of the time-averaged axial veloc- ity for each rotor configuration, normalized by the blade tip speed, as well as the corresponding velocity vectors along various radial cuts through the rotor wake. To limit image congestion only every 10th vector in the radial direction is displayed. It is important to note that the axis system for the current measurements was defined from the hub plane; blade flapping was not accounted for, which is why the blade appears above the $z/R = 0$ position. Figure 4.5 shows that each blade set produced a wake with a well-defined slipstream boundary, separating the high-velocity flow inside the wake from the quiescent flow outside the rotor wake. As expected, based off conservation of mass, in each case the contraction of the rotor wake resulted in the velocity in the wake increasing with downstream distance from the rotor.

Figures 4.5a and 4.5b show that the baseline and lowest amplitude blades produced relatively similar flow fields. Specifically, the axial velocity distribution was biased towards the blade tip, with the lowest velocities occurring inboard. Conversely, the higher amplitude blades (i.e., A = $0.05c$ and A = $0.12c$) produced a somewhat more uniform velocity distribution, with largest amplitude blade producing the most uniform velocity distribution.

To further examine the velocity distribution in the wake, the axial velocity along a radial cut through the hub plane (i.e., induced velocity, v_i) was extracted for each rotor configuration and

used to obtain the inflow ratio (i.e., $\lambda = v_i/V_{tip}$). Figure 4.6 shows the spanwise distribution of inflow for each blade. It is important to note that because the time-averaged measurements were obtained from averaging discrete phase-averages, the effect of the tip vortices on the inflow was not completely removed. Figure 4.6 shows that increasing protuberance amplitude resulted in the inflow distribution becoming more uniform. As was observed in the power polars (see Fig. 4.1), wavelength had minimal effect on the inflow distribution.

Blade element momentum theory (BEMT) states that a more uniform inflow distribution decreases induced losses, with minimum induced losses occurring for a completely uniform (ideal) inflow distribution [7]. Furthermore, a more uniform inflow distribution is most often achieved using linear nose-down blade twist. Compared to an untwisted blade, BEMT predicts that a linearly twisted blade will have higher inflow velocities inboard of $r = 0.75R$ and low velocities outboard, causing the inflow curves of each blade to intersect at $r = 0.75R$ (see Fig. 4.7) [7]. Examin- ing Fig. 4.6, inflow distribution produced by the higher amplitude blades mimic that of a linearly twisted blade, intersecting the baseline and low amplitude curves at approximately $r \approx 0.78R$. Although the largest amplitude blade produced a more uniform inflow distribution as compared to the other blades tested, it had the highest power requirements (see Fig. 4.1). Therefore, the additional power requirements of the modified blades would be expected to result from flow features which vary spatially with time and do not appear in the average flow field (i.e., streamwise vortices trailed from the protuberances).

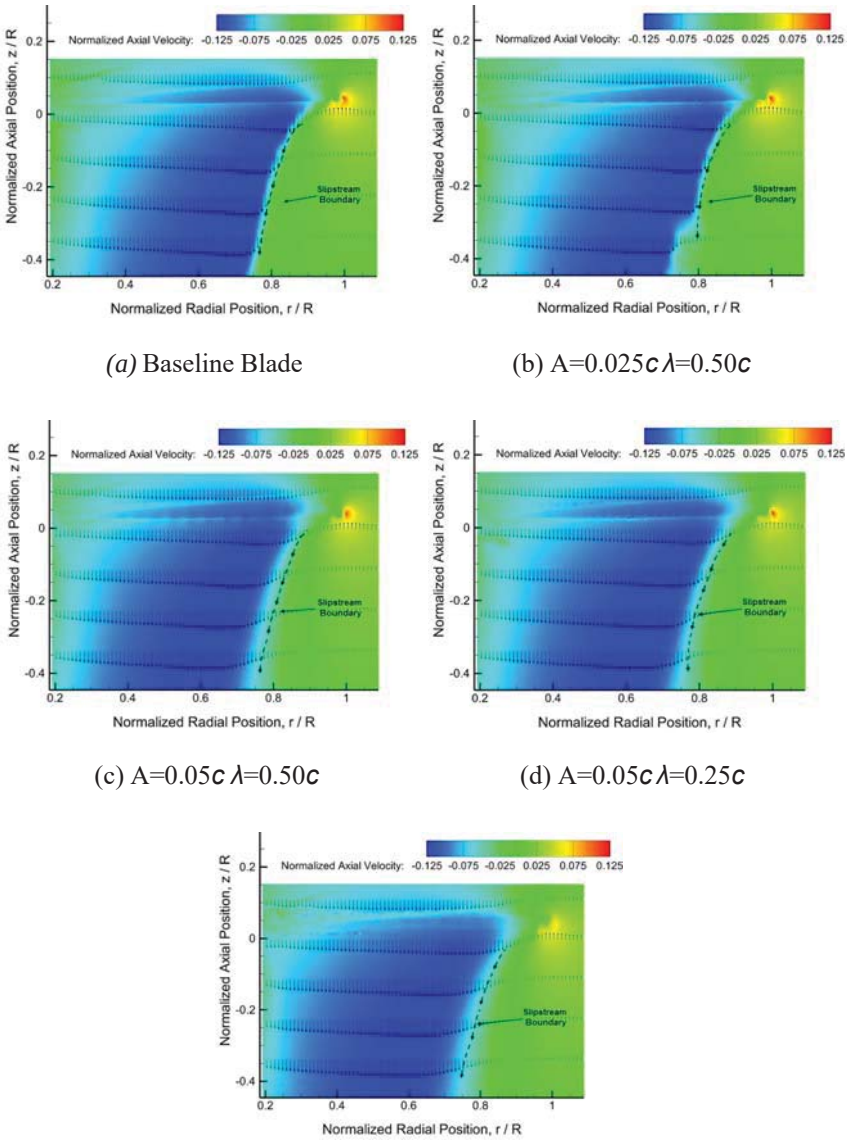

(a) Baseline Blade

(b) A=0.025c λ=0.50c

(c) A=0.05c λ=0.50c

(d) A=0.05c λ=0.25c

(e) A=0.12c λ=0.50c

Figure 4.5: Time-averaged contours of axial velocity normalized by the rotor tip speed for each blade geometry: (a) Baseline; (b) A=0.025c λ=0.50c; (c) A=0.05c λ=0.50c; (d) A=0.05c λ=0.25c; and (e) A=0.12c λ=0.50c.

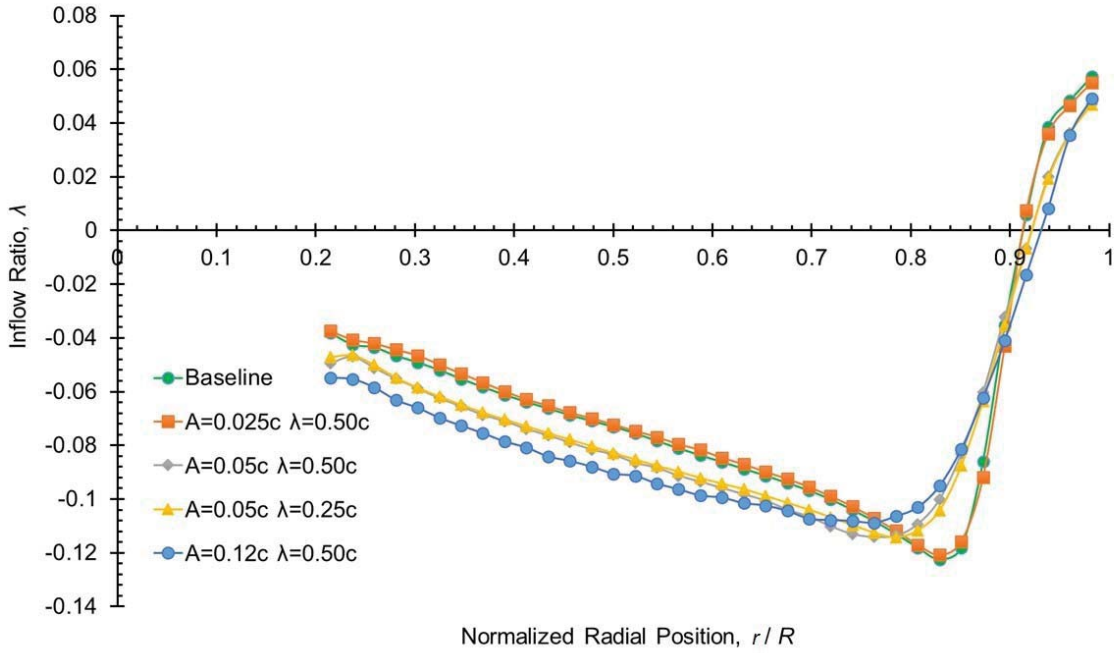

Figure 4.6: Plot of the measured spanwise inflow distribution for each blade geometry.

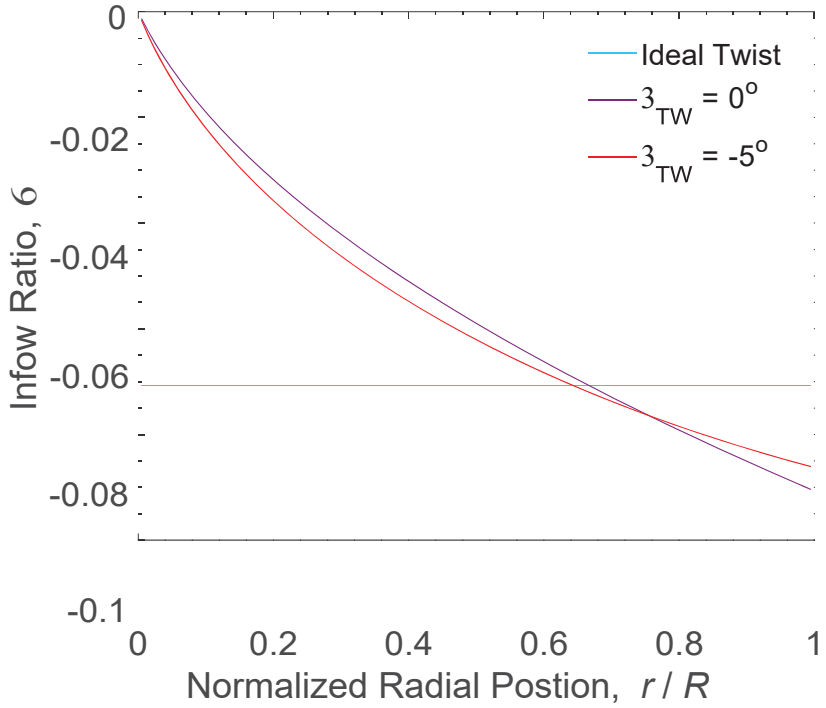

Figure 4.7: Blade element momentum theory prediction of the spanwise inflow distribution for an untwisted, ideally twisted, and linearly twisted blade.

4.3 Instantaneous Flow Field Measurements

In order to understand these flow features and view the wake structure at a moment in time, instantaneous images were analyzed. Figure 4.8 shows representative contours of instantaneous total velocity and the corresponding velocity vectors, normalized by rotor tip speed, for each rotor configuration at a blade azimuth position of $\Psi_b = 6^\circ$. To limit image congestion, only every 10th vector is displayed. While the tip vortex trailed from each blade initially induced local flow velocities greater than 30% of the tip speed, the vortices from the baseline and low amplitude blades were significantly more coherent. Specifically, the vortices generated by the baseline and low amplitude blades persisted in the wake to relatively late wake ages (i.e., $\zeta \geq 360^\circ$). As the vortices convected through the wake, minimal change in the vortex structure or flow velocities occurred, as shown in Fig. 4.8. Furthermore, the wake sheets trailed from the inboard sections of the blades were considerably weaker than the corresponding tip vortices (i.e., less than 35% of the tip vortices' peak velocities).

As compared to the baseline and low amplitude blades, the larger amplitude blades (A = 0.05c and A = 0.12c) produced significantly more intense wake sheets, with vortical structures that induced large regions of local flow velocities greater than 30% of the tip speed; see Fig. 4.8. The vortices in the wake sheet became more prominent beyond $r/R \approx 0.70$, with some being similar in size to the tip vortex. Furthermore, the larger amplitude blades also generated significantly less coherent tip vortices, which, after interacting with the wake sheet, persisted in the wake for less than one rotor revolution. Because power requirements scale with the cube of radial position, the creation of relatively large scale flow features outboard on the higher amplitude blades (compared to the generation of smaller, coherent tip vortices on the baseline blade) would be expected to sig-

nificantly increase the power requirements. As was also observed in the time-averaged flow fields (see Fig. 4.5), the higher amplitude blades produced a more uniform spanwise velocity distribution as compared to the baseline blade, with relatively high flow velocities inboard.

To further investigate the vortical nature of the rotor wake, contours of instantaneous vorticity were examined. Figure 4.9 shows contours of normalized instantaneous vorticity ($\omega c/\Omega R$) and velocity vectors corresponding to the representative realizations shown in Fig. 4.8. Vorticity, or the curl of velocity, is a measure of a fluid's rotation. This parameter is highlighted because it quantifies the strength of each vortex, as well as the air's interaction with the protuberances as those vortices are formed. As in previous figures, every tenth velocity vector is also displayed on each image.

Previous work by Ramasamey et al. [27] and Milluzzo and Leishman [28, 29] found that the wake sheets trailed from a rotor blade consisted of counter-rotating vortex pairs, often called Taylor–Görtler (T–G) vortices [30]. The T–G vortex pairs can be identified by the red (positive) and blue (negative) vorticity contours in Fig. 4.9, whereas the tip vortices appear as the larger regions of concentrated positive vorticity. Positive vorticity indicates counterclockwise rotation of the flow; negative vorticity contains clockwise rotation.

Figure 4.9 shows that, as compared to the vortices trailed from the higher amplitude blades, the tip vortices generated by the baseline and low amplitude blades persisted (in a significantly more coherent form) to later wake ages. Specifically, the primary source of vorticity in the downstream wake of the rotors with the baseline and lower amplitude blades was the tip vortex, with only minimal small scale vorticity present. Conversely, only traces of the tip vortices were present in the downstream wakes of the rotors with the higher amplitude blades; see Figs. 4.9c, 4.9d, and 4.9e. Furthermore, the interaction of these blades' wake sheets with the tip vortices resulted in

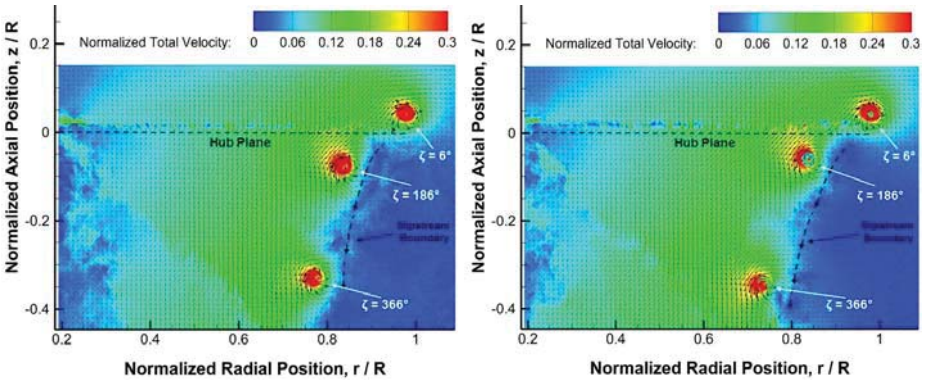

(a) Baseline Blade (b) A=0.025c λ=0.66c

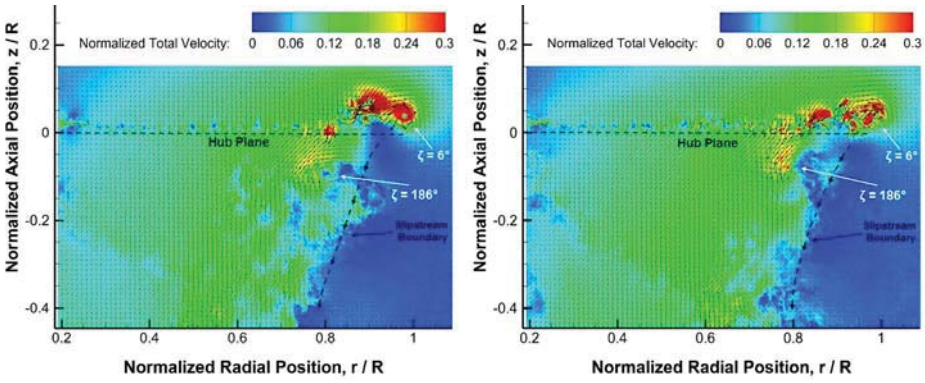

(c) A=0.05c λ=0.66c (d) A=0.05c λ=0.66c

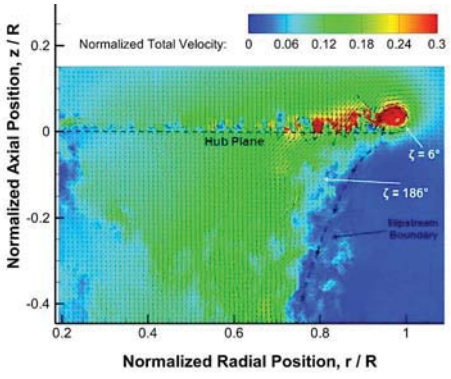

(e) A=0.12c λ=0.66c

Figure 4.8: Instantaneous contours of total velocity, normalized by the rotor tip speed, with the reference blade at $\Psi_b = 6^\circ$: (a) Baseline; (b) A=0.025c λ=0.50c; (c) A=0.05c λ=0.50c; (d) A=0.05c λ=0.25c; and (e) A=0.12c λ=0.50c.

significantly more turbulent wakes, with vorticity from the wake sheets bundling around the tip vortices along the slipstream boundary.

While the baseline and low amplitude blades appeared to have very similar flow fields (a concentrated tip vortex that persists in the wake and a less intense wake sheet), Fig. 4.9 shows some unique differences in the structure of the wake sheet. Specifically, the wake sheet trailed from the lower amplitude blade was thicker and contained relatively large vortical structures as compared to the baseline blade. Furthermore, at early wake ages, the wake sheet trailed from the lower amplitude blade also had a pronounced wave-like instability that formed along the entire length of the sheet. Milluzzo and Leishman [28] also noted the formation of wave-like instabilities in the wake sheets trailed from untwisted and relatively highly twisted rotor blades. These instabilities were expected to have been self-induced by the vortical flow features in the sheet, as well as caused by the wake sheet's interaction with the tip vortex. Therefore, the larger vortical structures present in the sheet generated by the lower amplitude blade likely induced a more pronounced instability; see Fig. 4.9b.

Compared to the baseline and low amplitude blades, the higher amplitude blades trailed a significantly more intense wake sheet, with vortical structures of similar size and vorticity to that of tip vortex; see Fig. 4.9. Furthermore, the size of the vortical structures trailed into the sheet and the magnitude of the wave-like instability formed on the sheet was directly related to the protuberance amplitude, with the highest amplitude blade (i.e., A12) generating the largest vortical structures and the highest magnitude instabilities; see Fig. 4.9e.

Milluzzo and Leishman [28] showed that the addition of twist to a rotor blade significantly increased the vorticity trailed into the wake sheet. Using predictions from a free-vortex method, they showed the increased vorticity in the wake sheet was most likely the result of modifications

to the spanwise distribution of bound circulation. Examining Fig. 4.9, leading-edge protuberances had a similar effect on the rotor wake as blade twist (i.e., an increase in vorticity trailed into the wake sheet). Therefore, the increased vorticity trailed from the modified blades suggests a potential modification to the spanwise distribution of bound circulation along the blades. Because the intensity of the wake sheets was directly related to the protuberance size, the highest amplitude blade would be expected to have the greatest effect on the distribution of bound circulation.

To understand the development and evolution of the rotor wake, later wake ages were also examined. Figure 4.10 shows representative contours of total velocity, normalized by tip speed, with the blade at an azimuth angle of $\Psi_b = 90^\circ$ for each rotor configuration. In the baseline case, two tip vortices are present, with the third convecting out of the region of interest. The baseline and lower amplitude blades had similar flow fields to those shown at $\Psi_b = 6^\circ$ (see Figs. 4.8a and 4.8b).

As previously discussed, the higher amplitude blades (A05, A05 HF, and A12) were found to produce tip vortices that dissipate rapidly. Whereas tip vortices induced velocities higher than 30% of the tip speed at $\Psi_b = 6^\circ$ (which was similar to the baseline), this was not the case at $\Psi_b = 90^\circ$. Figures. 4.10d and 4.10e show that these geometries producing vortex speeds less than 18% of the blade tip speed. As previously shown in the time-averaged inflow (see Fig. 4.6), the A05, A05 HF, and A12 blades produced more uniform inflow distributions. With higher velocities inboard of the tip, stronger wake sheets would be expected to form. In both the baseline and higher amplitude blades, the wake sheet convected faster than the corresponding tip vortex. However, in the higher amplitude cases, the wake sheet interacts with the tip vortex.

The velocity vectors show that there is still positive (counterclockwise) rotation present in the tip vortex at $\zeta = 90^\circ$. Below the hub plane ($z/R \leq -0.05$), turbulent vortical elements lead to an exchange of momentum across the slipstream boundary, causing a less defined boundary

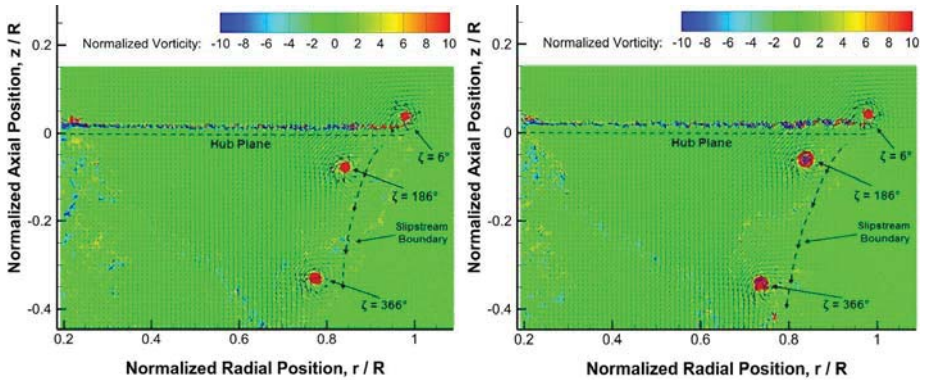

(a) Baseline Blade (b) A=0.025c λ=0.50c

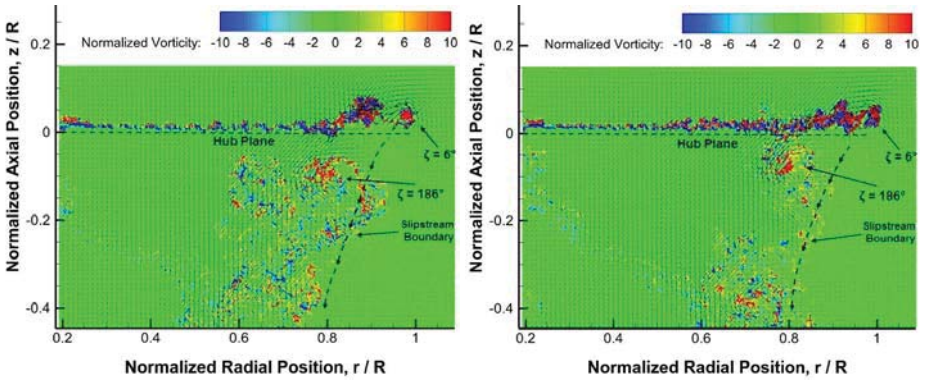

(c) A=0.05c λ=0.50c (d) A=0.05c λ=0.25c

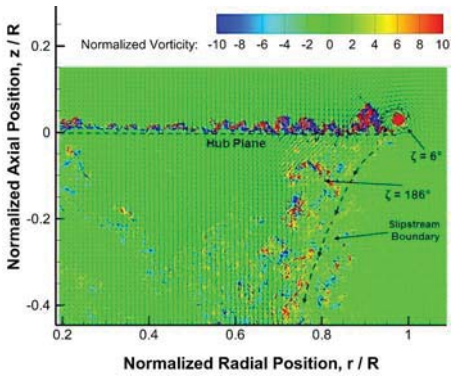

(e) A=0.12c λ=0.50c

Figure 4.9: Instantaneous contours of normalized vorticity, with the reference blade at $\Psi_b = 6^\circ$: (a) Baseline; (b) A=0.025c λ=0.50c; (c) A=0.05c λ=0.50c; (d) A=0.05c λ=0.25c; and (e) A=0.12c λ=0.50c.

compared to the baseline case. When the remnants of the initial tip vortex interact with these turbulent regions, the vortex is further weakened as the air in the wake resists turning. The weaker rotational components of the velocity were most pronounced in the flow field produced by the highest amplitude blade, where the wake becomes almost one-directional and extends inboard of $r/R = 0.2$ and below $z/r = -0.2$.

Figure 4.11 shows instantaneous vorticity contours at $\Psi_b = 90^\circ$ for each blade. In the baseline and A025 cases, two tip vortices are shown as the concentrated regions of positive vorticity. Each blade's wake sheet is shown as a thin region of weak, mostly negative vorticity extending from the hub to the $\zeta = 270^\circ$ vortex. Apart from these flow features, there was minimal vorticity in the baseline and low amplitude wakes.

The high amplitude blades exhibited more intense wake sheets, with a larger region of vorticity of similar magnitude to the tip vortex. This indicates that the higher amplitude blades generated wake sheets which were stronger than those produced by the lower amplitude blades. Thus, more intense negative vorticity was generated on the interior of these blades, most likely caused by the presence of higher amplitude protuberances. Regions of positive and negative vorticity were present in the wake outboard of $r/R = 0.6$; see Figs. 4.11c–4.11e.

It is interesting to note that while the wake sheet trailed negative vorticity into the inboard are of the wake (i.e., $r/R \leq 0.6$), there was a large amount of positive vorticity distributed throughout this region of the wake that was not present in the baseline case. Because the primary source of positive vorticity was generated at the tip, it is believed that the region of positive vorticity are remnants of the tip vortex, and the dissipation of the tip vortex is most likely cause by its interaction with the wake sheet; see Figs. 4.11c to 4.11e. The vorticity in the tip vortex entrained vorticity of the opposite sign to itself and caused the tip vortex's strength to diminish. Mitigated

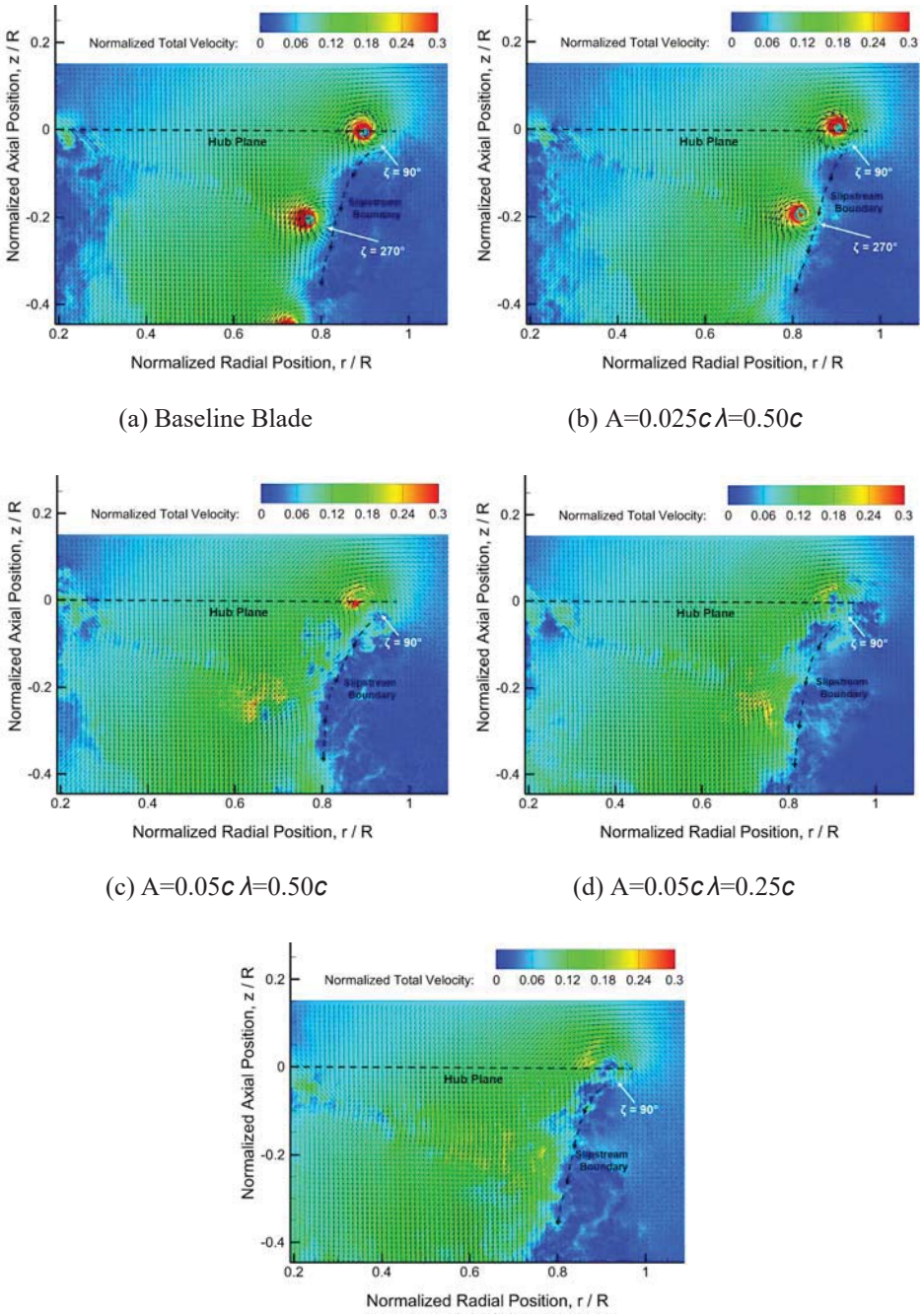

(a) Baseline Blade

(b) A=0.025c λ=0.50c

(c) A=0.05c λ=0.50c

(d) A=0.05c λ=0.25c

(e) A=0.12c λ=0.50c

Figure 4.10: Instantaneous contours of total velocity, normalized by the rotor tip speed, with the reference blade at $\Psi_b = 90^\circ$: (a) Baseline; (b) A=0.025c λ=0.50c; (c) A=0.05c λ=0.50c; (d) A=0.05c λ=0.25c; and (e) A=0.12c λ=0.50c.

tip vortices could reduce the negative consequences associated with their potenial interaction with an oncoming blade (see [31, 32]) or the ground during low alitude hover (see [33, 34]).

Analyzing the entire wake structure illustrates how tip vortices interact with other flow features and overall wake characteristics. As previously discussed, protuberances could potentially affect the distribution of bound circulation along the wake sheet. If that's the case, that would affect the trailed circulation and vorticity into the wake. To quantify these parameters, this study examined a section of the blade that encompassed a small portion of the wakesheet.

In order to further analyze the characteristics of the vortical flow along the rotor blade, the vortices in all 300 instantaneous images must be collocated; that is, the centers of each tip vortex must be aligned at the same wake age before phase averaging. However, this cannot be achieved since the flow under examination contains aperiodic elements, namely the varying spatial location of each vortex. An effort was thus begun to isolate the instantaneous, transient artifacts of the flow field from the phase-averaged characteristics. A Reynolds decomposition method was chosen to extract the transient structures within the flow (the vortex) from the mean surrounding flow. By subtracting the average flow field, the fluctuations can be visualized.

Figure 4.12 shows the instantaneous normalized vorticity contours at $\Psi_b = 6^\circ$ for all rotor configurations. The vectors show the phase-averaged total velocity subtracted from instantaneous values. These images show representative sections of the wake sheet at a smaller scale (i.e., 5% of the radius), which allows for closer inspection of the wake sheets and their distinct areas of vorticity. The baseline case shows with postive and negative vortical flow present along the radius. These counter-rotating vortex pairs are often called Taylor–Görtler (T–G) vortices and are common among rotor blades with various geometries; see [27–30]. The velocity vectors turn inboard across the strip of vorticity as it begins to contract through the wake.

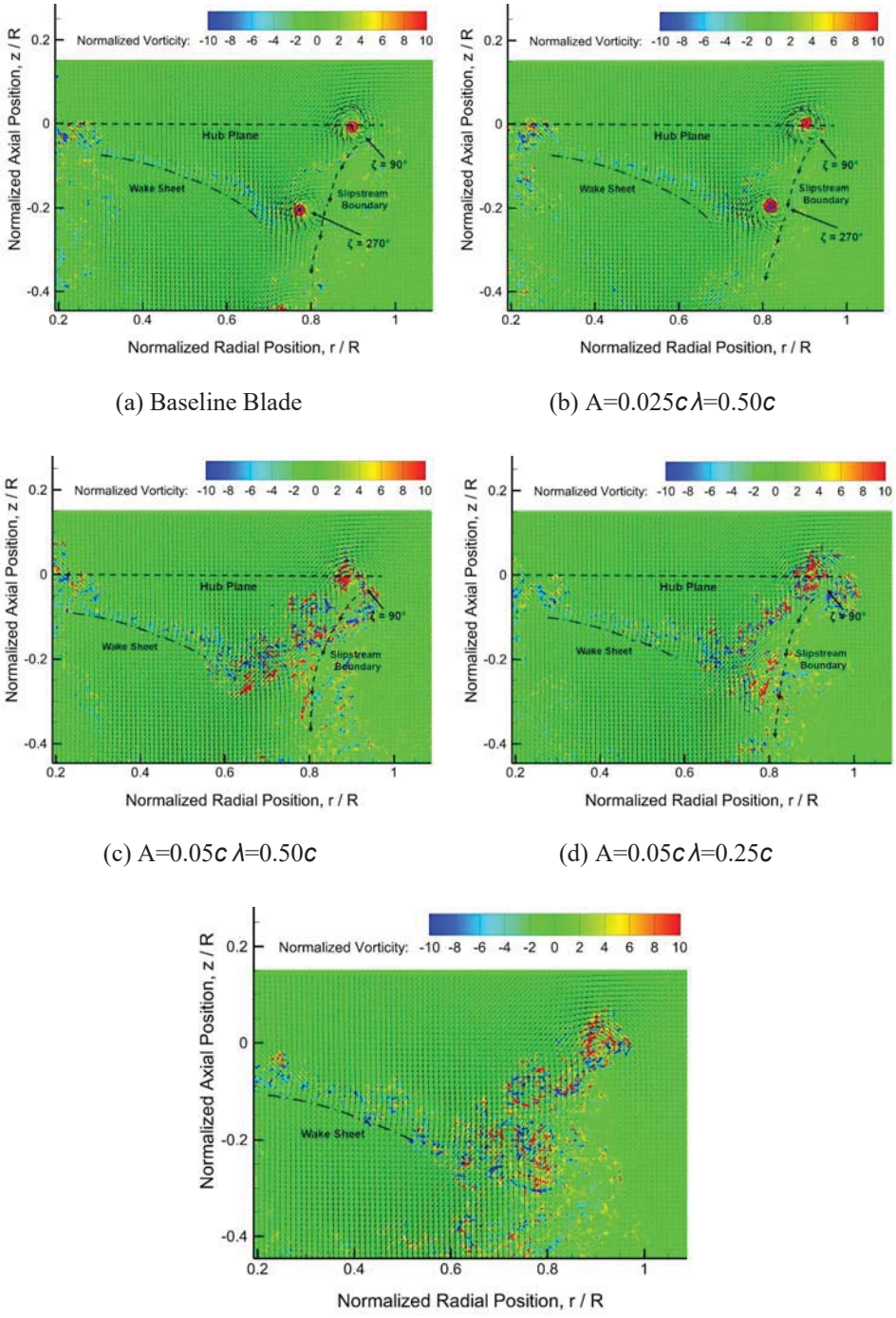

(a) Baseline Blade

(b) A=0.025c λ=0.50c

(c) A=0.05c λ=0.50c

(d) A=0.05c λ=0.25c

(e) A=0.12c λ=0.50c

Figure 4.11: Instantaneous contours of total vorticity, with the reference blade at $\Psi_b = 90^\circ$: (a) Baseline; (b) A=0.025c λ=0.50c; (c) A=0.05c λ=0.50c; (d) A=0.05c λ=0.25c; and (e) A=0.12c λ=0.50c.

In the A05 blade's vorticity distribution, the strip of vorticity undulates across the radius and two peaks can be seen clearly at $r/R = 0.60$ and $r/R = 0.65$. The areas of positive and negative vorticity appear to alternate along the radial section shown. Below the hub plane at $z/R = 0$, the velocity vectors turn inboard, but the directions of the velocity vectors across the vorticity region varies. The alternating pockets of positive and negative vorticity in the instantaneous images are most likely caused by the protuberances; however, it is unclear whether the vorticity is a result of vortical flow or merely flow turning around the protuberances as it flows through the rotor disk. These differences can be significant: whereas flow turning around the protuberances shows that the geometric features merely influence the direction of the flow through the rotor, true vortex production would indicate a change in the flow's momentum and circulation along the radius.

Figure 4.12d shows the vorticity of the A05 HF blade's flow field. Pockets of positive vorticity are present along the radius of the blade. Their size is smaller, reflecting the higher frequency of the protuberances. The tip vortex and its propagation through the wake are similar to the low frequency A05 blade. Thus, while protuberance wavelength alters the local fluid interaction with protuberances (i.e., smaller pockets of vorticity), wavelength does not have an impact on tip vortex structure or performance; see Fig. 4.1.

4.4 Phase-Averaged Flow Field Measurements

Phase-averaged flow field measurements were taken for each blade at different blade azimuth angles. Three hundred images were averaged at each blade azimuth angle, illustrating the wake structures without transient effects such as turbulence or aperiodic flow features. While phase-averaged vorticity measurements do not provide insight into the instantaneous behavior shown in

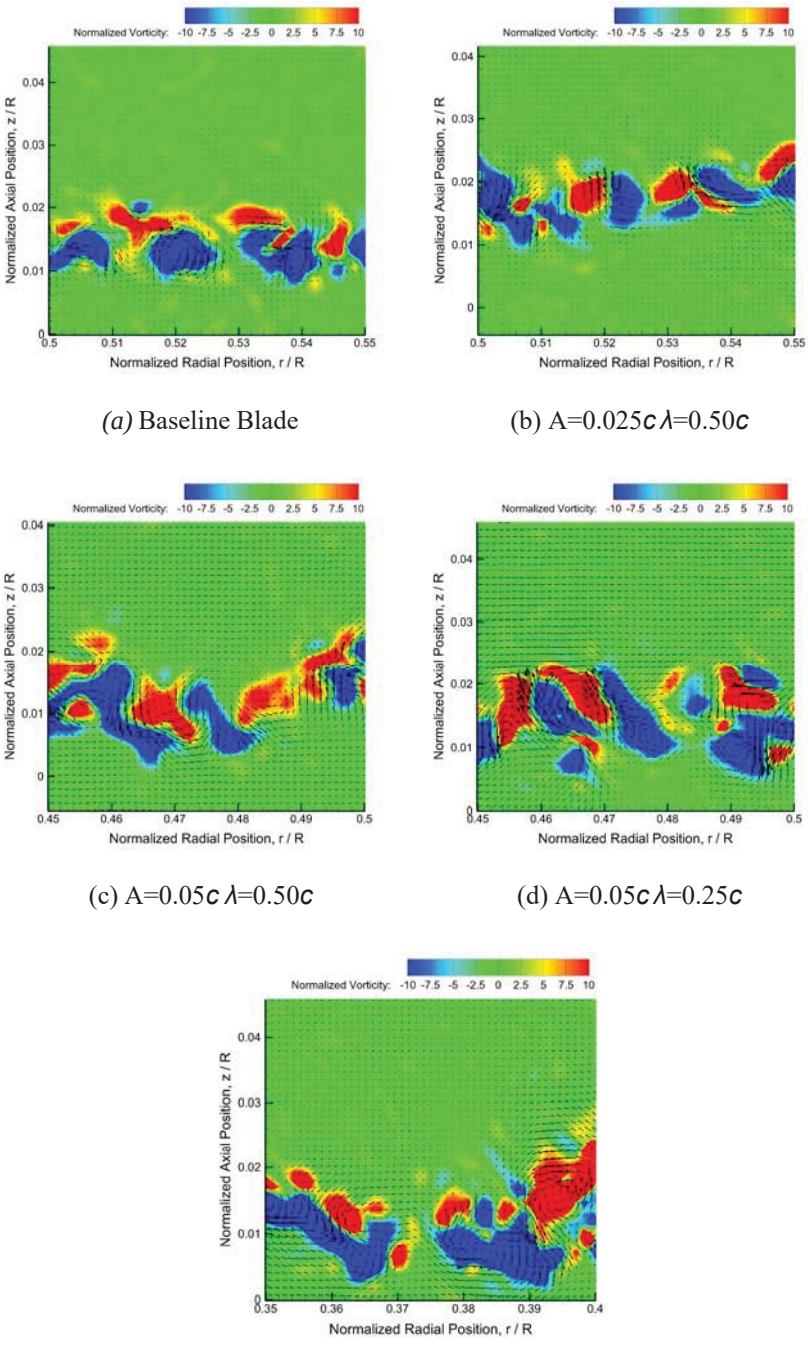

(a) Baseline Blade

(b) A=0.025c λ=0.50c

(c) A=0.05c λ=0.50c

(d) A=0.05c λ=0.25c

(e) A=0.12c λ=0.50c

Figure 4.12: Contours of instantaneous-minus-average normalized vorticity, with the reference blade at $\Psi_b = 6^\circ$: (a) Baseline; (b) A=0.025c λ=0.50c; (c) A=0.05c λ=0.50c; (d) A=0.05c λ=0.25c; and (e) A=0.12c λ=0.50c.

previous figures, they provide an understanding of the average characteristics of the wake. Figures 4.13–4.17 also contains the blade's leading-edge sinusoidal geometry for reference, located at a position 3% above the 0° hub plane. All early wake ages (i.e., 3° to 30°) are shown to focus on the creation of the wake sheet (where it is strongest) before it dissipates through the rest of the wake.

Figure 4.13 shows contours of normalized vorticity present along the radius of the baseline blade. At $\zeta = 3°$, a solid region of positive vorticity lies above a solid region of negative vorticity. This indicates that the flow first turns in a counterclockwise direction, then clockwise direction as it continues through the wake. The tip vortex rolls cleanly off the blade tip. At $\zeta = 6°$, the positive region begins to dissipate while the negative region remains at about the same strength. More dissipation occurs at later wake ages, with the positive region only present in the tip region (outboard of $r/R = .90$) at $\zeta = 30°$. In contrast, stronger negative vorticity remains in the region of interest throughout the wake ages shown.

Figure 4.14 shows the A025 blade with phase-averaged vorticity contours across all early wake ages. Previously, performance and time-averaged flow field measurements showed very similar features between the baseline and A025 blades, suggesting that a modified blade with protuberances of relatively small amplitude does not influence flow mechanisms. However, Fig. 4.14 shows that the low amplitude blade had a significant change in the vorticity of the average wake sheet. The low amplitude blade had a wave-like instability form along its radius as seen in the higher amplitude blades. This was consistent with the results from the medium amplitude blades, which showed that protuberance wavelength is insignificant in affecting the flow; the only difference was shown in the vorticity contours.

Figure 4.15 shows more pronounced vorticity pockets than the low amplitude blade. From

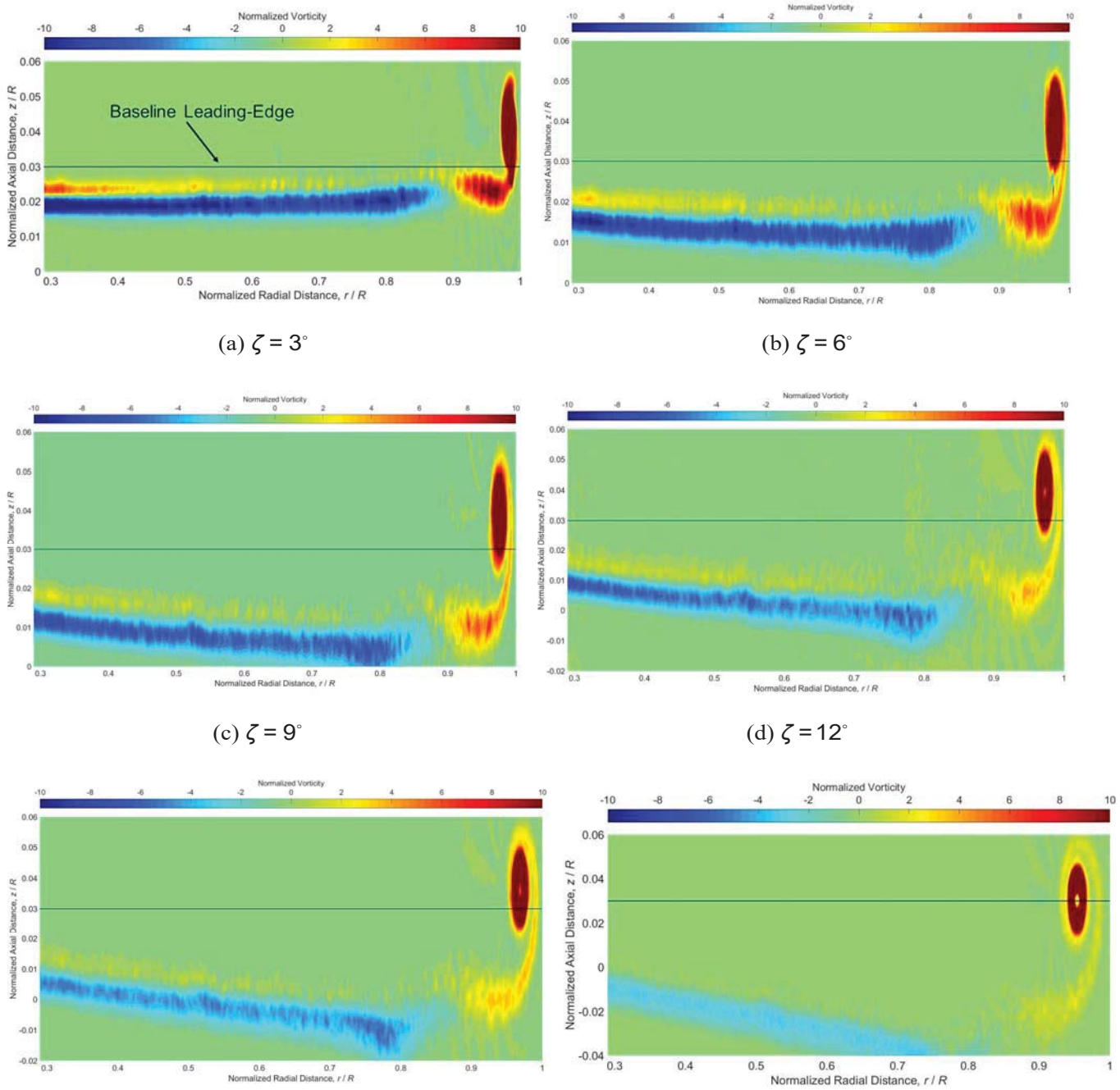

(a) $\zeta = 3^{\circ}$

(b) $\zeta = 6^{\circ}$

(c) $\zeta = 9^{\circ}$

(d) $\zeta = 12^{\circ}$

(e) $\zeta = 15^{\circ}$

(f) $\zeta = 30^{\circ}$

Figure 4.13: Phase-averaged vorticity distributions along the radius of the baseline blade at early wake ages: (a) $\zeta = 3^{\circ}$; (b) $\zeta = 6^{\circ}$; (c) $\zeta = 9^{\circ}$; (d) $\zeta = 12^{\circ}$; (e) $\zeta = 15^{\circ}$; and (f) $\zeta = 30^{\circ}$.

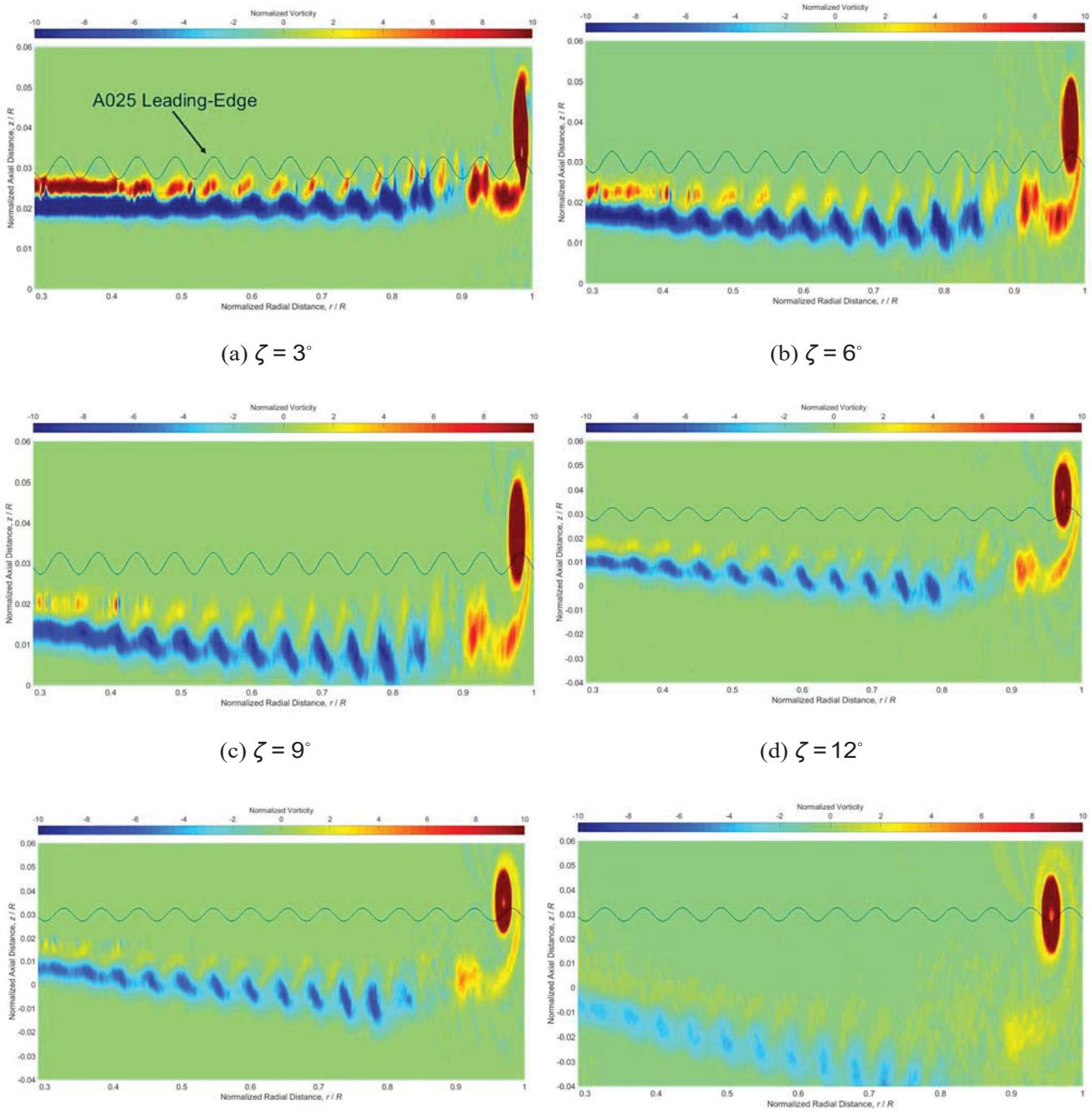

(a) $\zeta = 3^{\circ}$ (b) $\zeta = 6^{\circ}$

(c) $\zeta = 9^{\circ}$ (d) $\zeta = 12^{\circ}$

(e) $\zeta = 15^{\circ}$ (f) $\zeta = 30^{\circ}$

Figure 4.14: Phase-averaged vorticity distributions along the radius of the A025 blade at early wake ages: (a) $\zeta = 3^{\circ}$; (b) $\zeta = 6^{\circ}$; (c) $\zeta = 9^{\circ}$; (d) $\zeta = 12^{\circ}$; (e) $\zeta = 15^{\circ}$; and (f) $\zeta = 30^{\circ}$.

$\Psi_b = 0^\circ$ to 15°, layers of positive and negative vorticity are present along the blade. In the positive layer, sections of intense vorticity are scattered across the wake sheet and are separated by small regions of weaker vorticity. Beyond $\Psi_b = 15^\circ$, these regions lose their intensity, although the stronger tip vortex still persists. These regions have a length of about 5% of the radius, which is the same wavelength of the protuberances. It may be possible, therefore, to change the protuberance geometry in such a way to optimize the production of vorticity to achieve the desired distribution. These elements are present for the length of the interior of the blade until approximately $r/R = 0.70$. The tip vortex is indicated by the region of positive vorticity; it is adjacent to a region of weaker, more diffuse positive vorticity in the outboard 20% of the blade. This region is not present at $\Psi_b = 30^\circ$, suggesting that the formation of the tip vortex is influence by a turbulent wake sheet which is not present once the blade position is not shown in the image.

In Fig. 4.16, the A05 HF blade's vorticity distribution whose wavelength is reduced by half. Thus, there appears to be a correlation between protuberance wavelength and the wavelength of the alternating positive and negative vorticity pairs. Additionally, these pairs are less distinct compared to the baseline, A025, and A05 vorticity distributions. This is most likely a result of the phase-average . In each image, these pairs were not at identical positions along the radius, and the smaller wavelength of their distribution created stronger interactions between them. Thus, when averaged across the entire phase, the vortex pairs were "smeared," resulting in less coherence than seen in wake sheets of the lower amplitude blades.

Fig. 4.17 shows images of the A12 blade with phase-averaged vorticity contours across all early wake ages. Similar to the A05 HF blade, larger vortical elements along the radius resulted in averaged vorticity elements that are less coherent than those produced by smaller amplitude blades. Figure 4.17 illustrates that, as blade amplitude increases, the vorticity pockets along the hub plane

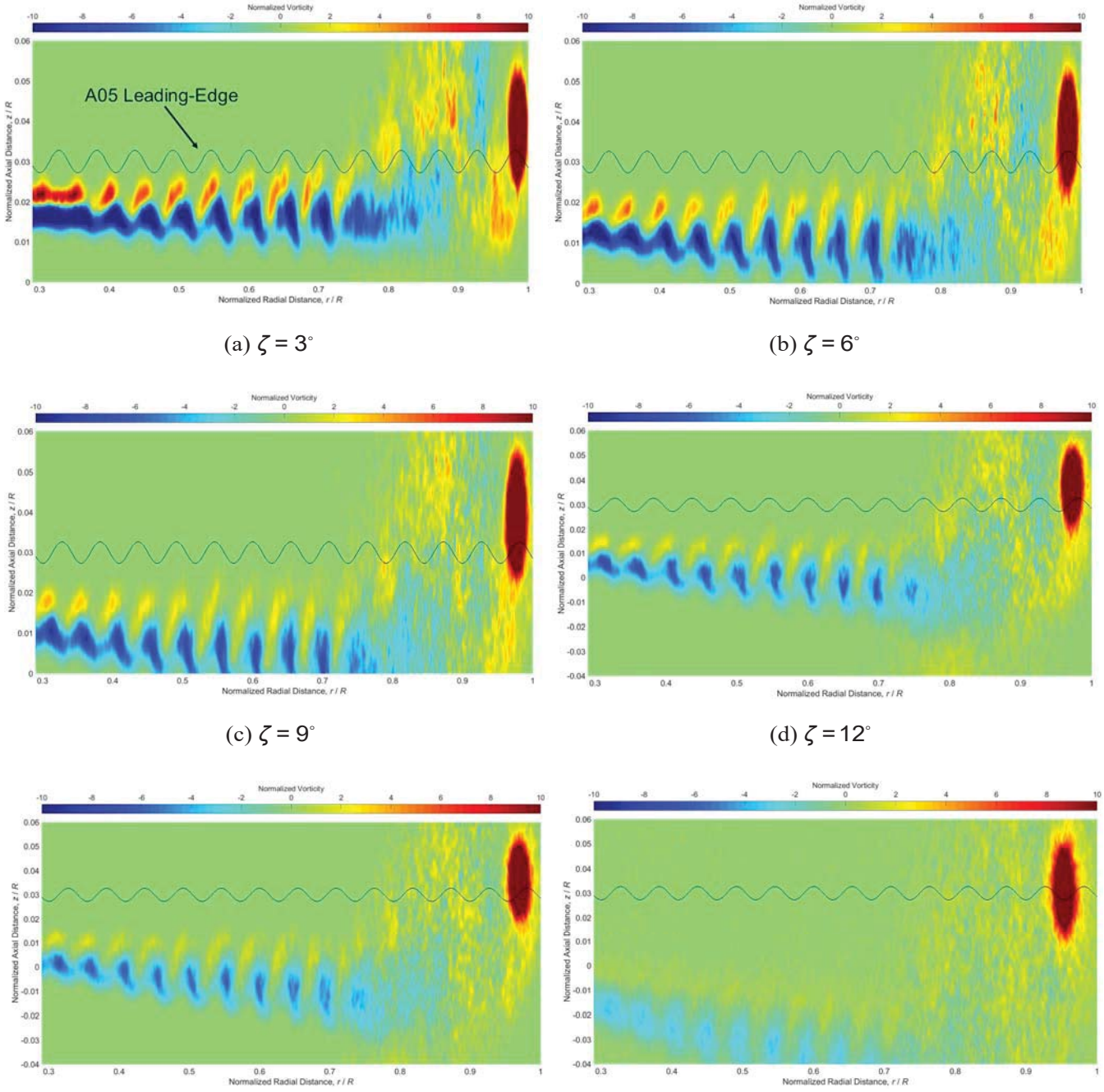

(a) $\zeta = 3^{\circ}$ (b) $\zeta = 6^{\circ}$

(c) $\zeta = 9^{\circ}$ (d) $\zeta = 12^{\circ}$

(e) $\zeta = 15^{\circ}$ (f) $\zeta = 30^{\circ}$

Figure 4.15: Phase-averaged vorticity distributions along the radius of the A05 blade at early wake ages: (a) $\zeta = 3^{\circ}$; (b) $\zeta = 6^{\circ}$; (c) $\zeta = 9^{\circ}$; (d) $\zeta = 12^{\circ}$; (e) $\zeta = 15^{\circ}$; and (f) $\zeta = 30^{\circ}$.

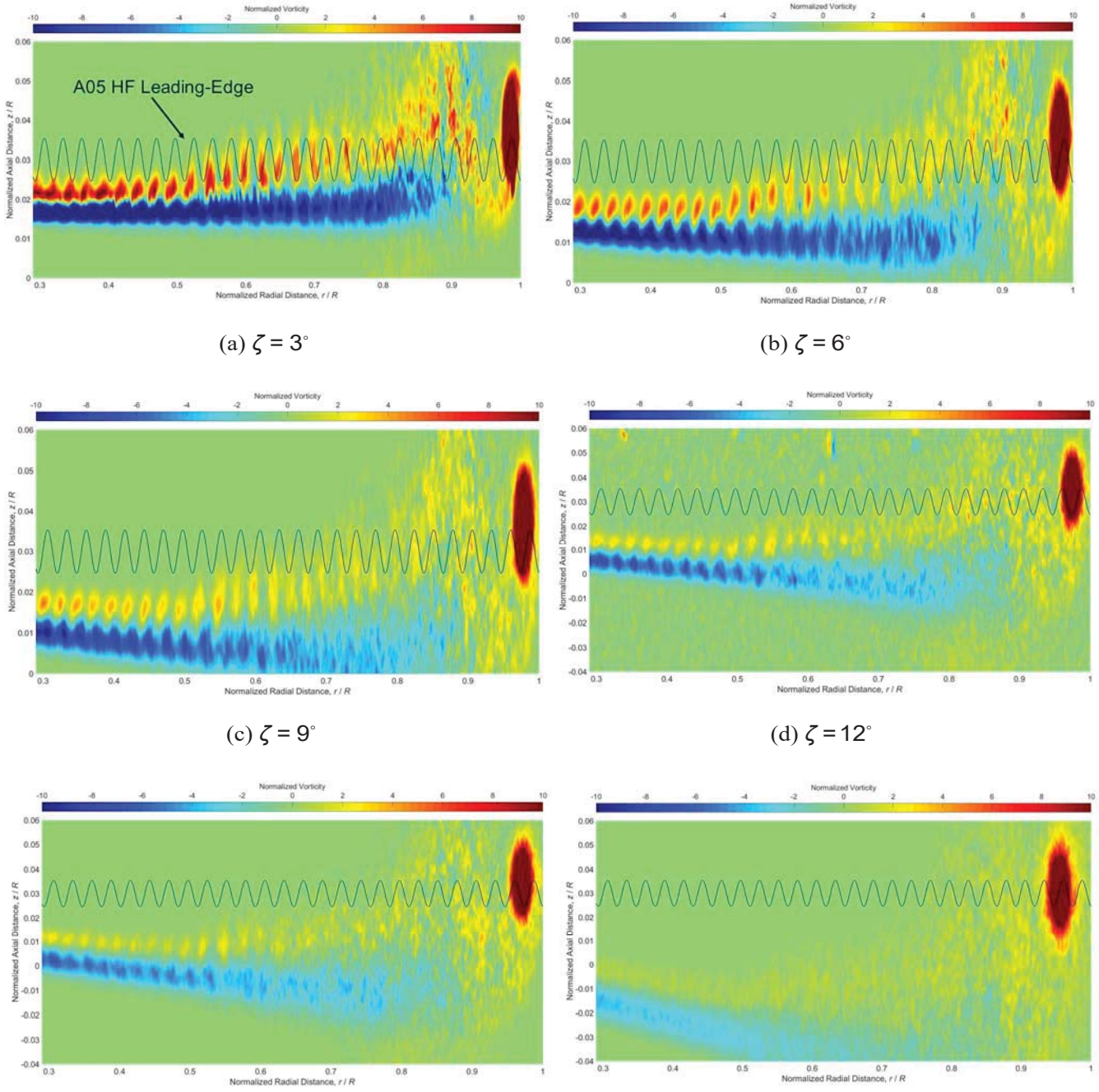

(a) $\zeta = 3^{\circ}$

(b) $\zeta = 6^{\circ}$

(c) $\zeta = 9^{\circ}$

(d) $\zeta = 12^{\circ}$

(e) $\zeta = 15^{\circ}$

(f) $\zeta = 30^{\circ}$

Figure 4.16: Phase-averaged vorticity distributions along the radius of the A05 HF blade at early wake ages: (a) $\zeta = 3^{\circ}$; (b) $\zeta = 6^{\circ}$; (c) $\zeta = 9^{\circ}$; (d) $\zeta = 12^{\circ}$; (e) $\zeta = 15^{\circ}$; and (f) $\zeta = 30^{\circ}$.

become larger and are located higher above the plane. This possibly indicates that larger vortices are produced at the protuberances at all positions of the blade. With greater vorticity present inboard, it is expected that the tip vortex is weaker because bound circulation remains constant. An offloaded tip is beneficial for improving efficiency, which is counter to what was shown in the degraded performance measurements of the higher amplitude blades. Thus, the power penalty is expected to come from the generation of vortices at the protuberance sites; while the phase-averaged images indicate that this is a possibility, an analysis of instantaneous images can confirm the presence and strength of these vortices.

4.5 Vortex Characteristics

The tip vortices were also quantified using phase-averaged velocity profiles along horizontal cuts through the vortex core, often referred to as swirl velocity profiles. Because rotor wakes are naturally aperiodic, accurate average velocity profiles could not be obtained without correcting for this aperiodicity [35–41]. Ramasamy and Bhagwat [38] showed that a global correction method minimized the uncertainty associated with identification of the vortex center. Therefore, the current work used a global correction method applied over 300 instantaneous flow field realizations to obtain the swirl velocity profiles for each blade at each wake age. Figure 4.18 shows the phase-averaged swirl velocity profiles of the tip vortices generated by each blade for $30^\circ \leq \zeta \leq 150^\circ$. The profiles are displayed in terms of normalized radial position, r/R, from the rotational axis of the rotor, with $r/R = 1$ being the rotor blade tip. It is important to note that the convection of the tip vortices in the wake resulted in an asymmetry in the velocity profiles when viewed in a fixed reference frame (i.e., with respect to the rotor). However, a symmetric profile was obtained by

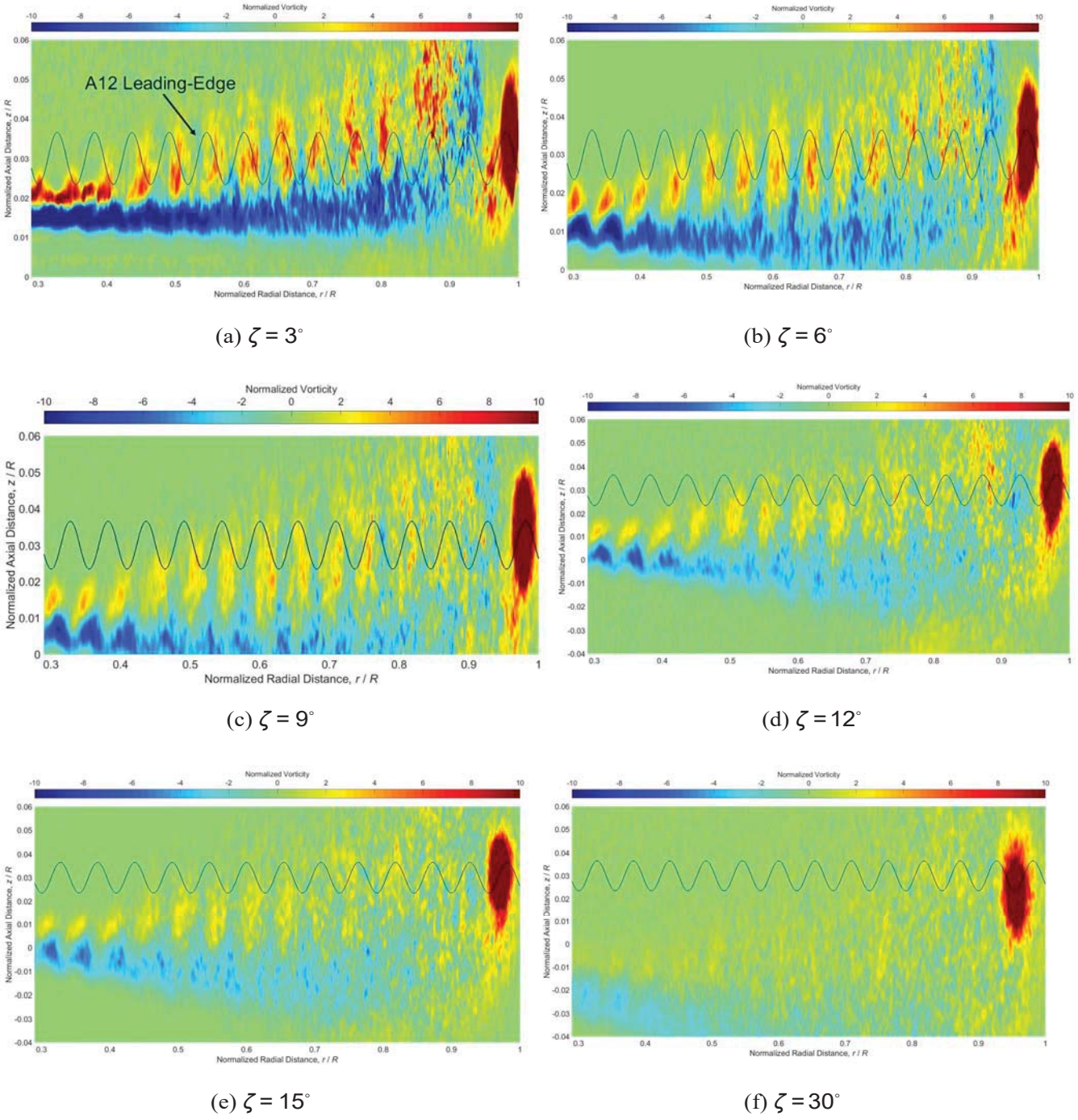

(a) $\zeta = 3^{\circ}$

(b) $\zeta = 6^{\circ}$

(c) $\zeta = 9^{\circ}$

(d) $\zeta = 12^{\circ}$

(e) $\zeta = 15^{\circ}$

(f) $\zeta = 30^{\circ}$

Figure 4.17: Phase-averaged vorticity distributions along the radius of the A12 blade at early wake ages: (a) $\zeta = 3^{\circ}$; (b) $\zeta = 6^{\circ}$; (c) $\zeta = 9^{\circ}$; (d) $\zeta = 12^{\circ}$; (e) $\zeta = 15^{\circ}$; and (f) $\zeta = 30^{\circ}$.

removing the convection velocity, as shown in Fig. 4.18.

Examining Fig. 4.18, the peak swirl velocity of the vortices trailed from each blade decreased with wake age, which was caused by the radial diffusion of vorticity away from the vortex core. Because tip vortices convect along the slipstream boundary, the contraction of the wake caused a radially inward shift of the swirl velocity profiles. It is interesting to note that by a wake age of 150°, the wakes of the higher amplitude blades (i.e., A05, A05 HF, and A12) contracted approximately 4% more than the wakes of the baseline and low amplitude blades. Moreover, the velocity profiles induced by the tip vortices from the baseline and low amplitude blades were very similar in magnitude, radial vorticity diffusion, and vortex spatial position; see Figs. 4.18a and 4.18b.

As shown in Figs. 4.8 and 4.9, the higher amplitude blades produced significantly more diffused tip vortices that induced lower flow velocities. Specifically, at $\zeta = 30^\circ$, the peak swirl velocities of the vortices generated by the higher amplitude blades were approximately 30% less than the baseline or low amplitude blade; see Fig. 4.18. Furthermore, the vortices from the higher amplitude blades diffused rapidly, and by $\zeta = 150^\circ$ their peak swirl velocities were approximately 70% lower than the baseline or low amplitude blades.

The peak swirl velocities of the phase-averaged tip vortex cuts were extracted and are plotted versus wake age in Fig. 4.19. The baseline vortex's peak velocity initially increases because it is still in the roll-up process; this is shown in work by Duaisamy et. al in [42]. Once the vortex is fully formed ($\zeta > 9^\circ$), the baseline case shows a similar trend to that of the other vortices: that is, a reduction in peak swirl velocity associated with a dissipation of the vortex, followed by more gradual dissipation for $\zeta \geq 60^\circ$. The baseline and A025 velocity curves show less reduction in V_{peak} because these blades produced more coherent tip vortices that persisted longer; see Figs. 4.8 and 4.10. The baseline and low amplitude blades retained the greatest peak velocities, with V_{peak}

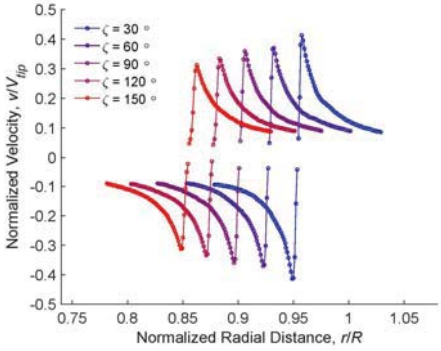

(a) Baseline Blade

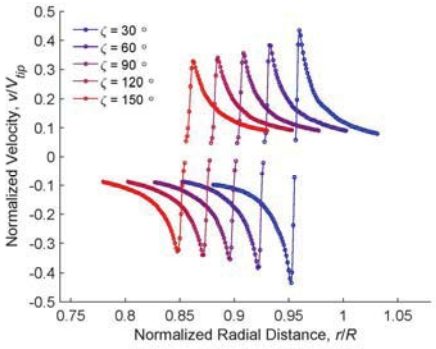

(b) A=0.025c λ=0.50c

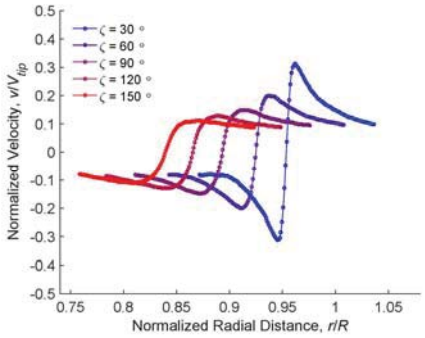

(c) A=0.05c λ=0.50c

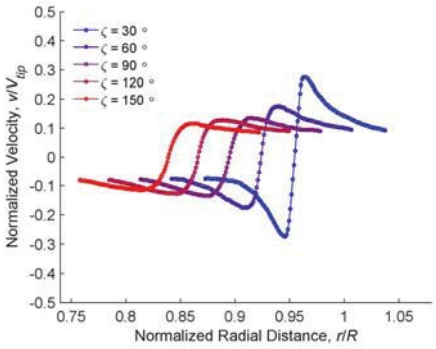

(d) A=0.05c λ=0.25c

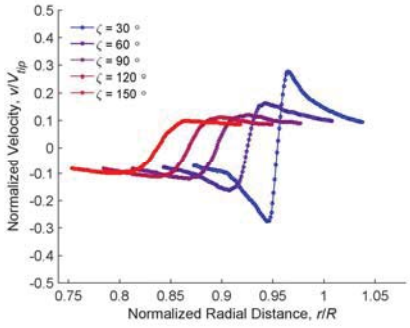

(e) A=0.12c λ=0.50ce

Figure 4.18: Phase-averaged velocity signatures of the tip vortex for each blade geometry: (a) Baseline; (b) A=0.025c λ=0.50c; (c) A=0.05c λ=0.50c; (d) A=0.05c λ=0.25c; and (e) A=0.12c λ=0.50c.

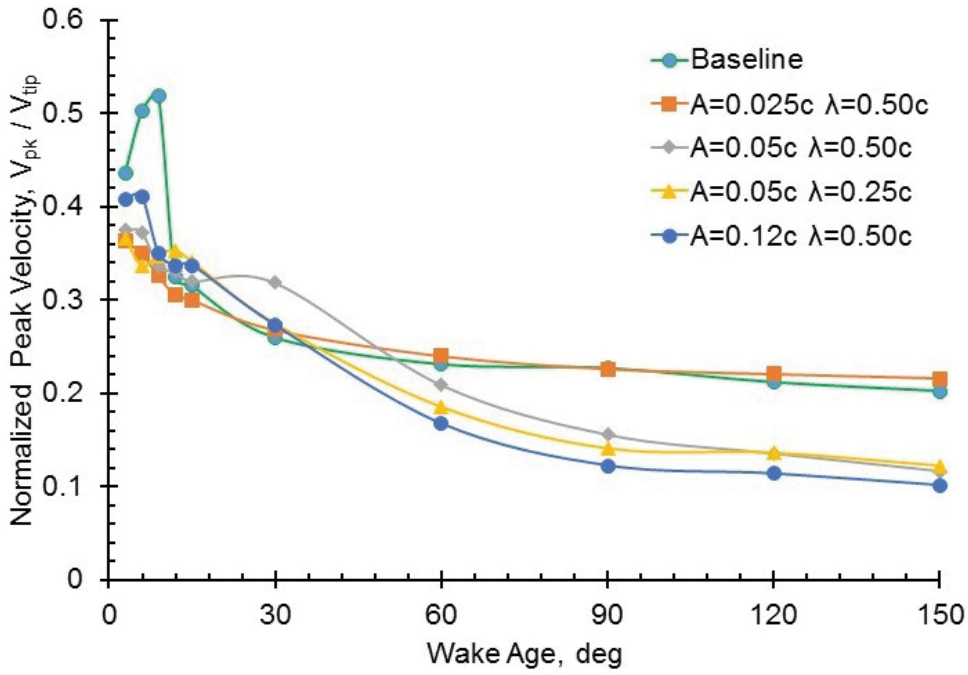

Figure 4.19: The normalized peak velocity of the tip vortex at various wake ages for each blade.

about 22% of the blade tip speed. The higher amplitude blades had the largest loss in peak swirl velocity. The A05 and A05 HF blades reached $V_{peak} = 14\%$ at $\zeta = 150^{\circ}$. The high amplitude blade's tip vortex was so diffuse in the phase-averaged image that it did not have a significant peak swirl velocity; at $\zeta = 120^{\circ}$, its speed was less than the medium amplitude blades at $V_{peak} = 12\%$.

4.6 Circulation Measurements

Lastly, the tip vortex circulation was calculated using the area integral of vorticity. Figure4.20 shows the circulation contained in each blade's tip vortex in wake ages ranging from $\zeta = 3^{\circ}$ to 150°. Across these wake ages, the baseline and low amplitude blades have approximately the same tip circulation values. This is most likely because the relatively weak vorticity in their wake sheets did not contribution significantly to circulation at the tip. In contrast, the tip vortices produced by

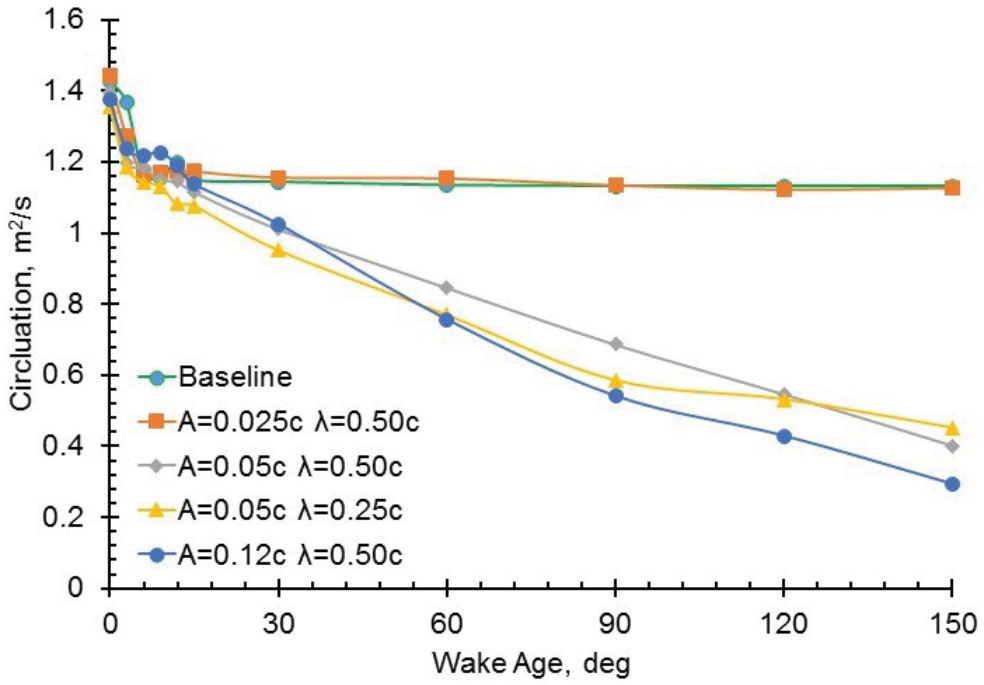

Figure 4.20: The normalized circulation of the tip vortex at various wake ages for each blade.

the higher amplitude blades interacted with the wake sheet. Specifically, those vortices entrained vorticity of the opposite sign to themselves, resulting in the 50% reduction in tip circulation seen in Fig. 4.20. The A05, A05 HF, and A12 blades produced tip vortices whose circulation decreased linearly as the wake age increased. Larger blade amplitude was directly related to a greater decrease in tip vortex circulation.

CONCLUSIONS

This work sought to gain an initial understanding of the effects protuberances have on hovering rotors, specifically their impact on performance, wake structure, and circulation. Performance and phase-resolved particle image velocimetry measurements were conducted on a rotor, operating out of ground effect, to gain insight into the wakes generated by blades with leading-edge protuberances. The effects of protuberance amplitude and wavelength were examined using four sets of blades with various sinusoidal leading-edges, as well as a baseline set of rectangular blades. Emphasis was placed on characterizing the initial structure of the tip vortices and wake sheets, as well as the average inflow through the rotor. From this work, the following conclusions havebeen obtained:

1. At relatively low thrust conditions (i.e., $C_T/\sigma \leq 0.06$), the protuberances were found to have a minimal effect on rotor performance, with the baseline and modified blades requiring similar power. As rotor thrust was increased the power requirements of the modified blades began to diverge from the baseline. Specifically, at the higher thrust conditions, the modified blades required more power to produce the same thrust.

2. The additional power requirements of the modified blades were directly related to protuberance amplitude. In particular, the largest amplitude blade deviated from baseline performance at the lowest thrust condition (i.e., $C_T/\sigma \approx 0.07$), which resulted in it having the greatest power requirements. The additional power requirements of the modified blades were hypothesized to stem from losses associated with the formation of streamwise vorticity

from the protuberances, which manifested as an increase in the induced power factor of the rotor. Furthermore, wavelength was found to have minimal effect, with the higher and lower frequency blades having similar power requirements.

3. The time-averaged flow fields of the baseline and low amplitude blades were relatively similar, with the spanwise distribution of axial velocity being biased towards the blade tip. Conversely, as protuberance amplitude was increased the velocity distribution became more uniform. As observed in the performance measurements, wavelength was also found to have a minimal effect on the average flow field.

4. The baseline and low amplitude blades were also found to produce similar instantaneous flow fields, i.e., less turbulent wake sheets and concentrated tip vortices that persisted to relatively late wake ages. Conversely, the higher amplitude blades were found to produce significantly more intense wake sheets. Furthermore, the tip vortices trailed from the higher amplitude blades were found to be less coherent, often persisting for less than one rotor revolution. These observations were confirmed in the phase-averaged swirl velocity profiles. Specifically, at $\zeta = 30^{\circ}$, the peak swirl velocity of vortices trailed from the higher amplitude blades were 30% lower than the baseline, and diffused at a considerably faster rate.

5. Vorticity was distributed along the radius of all blades in the form of counter-rotating vortices, which were visualized by subtracting phase-averaged velocity from instantaneous velocity. These regions were stronger and more pronounced in the higher amplitude blades compared to the baseline. Additionally, each modified blade contained a wake sheet that had a wave-like pattern across the radius. The wavelength of the alternating positive and negative vortical regions was equal to the wavelength of the protuberances of that blade. The

tip vortices produced by the modified blades entrained vorticity from the wake sheet (which was of opposite sign), which resulted in a 50% reduction of tip circulation at $\zeta = 150^{\circ}$.

GLOSSARY

Airfoil	The shape of the cross-section of a wing. In wind tunnel tests, an airfoil spans the full length of the test section. Also known as an infinite wing.
Angle of attack, α	The angle between the chord line of an airfoil and the horizontal freestream velocity.
Chord, c	The imaginary straight line connecting the leading- and trailing-edges of an airfoil.
Circulation, Γ	The amount of vorticity in a defined area. Circulation is directly related to lift generated.
Coefficient of lift, C_l	Dimensionless representation of lift generated by a lifting body.
Coefficient of power, C_P	Dimensionless representation of the rate of useful work generated by a turbine or required by a rotor.
Coefficient of thrust, C_T	Dimensionless representation of propulsive force generated by a turbine or rotor.
Coefficient of drag, C_d	Dimensionless representation of drag force on an object.
Flow separation	Detachment of a flows boundary layer over a surface. Separation occurs when the flow loses the energy to overcome the high pressure it encounters near the trailing-edge. Excess separation over a sufficient portion of a surface results in stall.

NACA	The National Advisory Committee for Aeronautics. This was a federal agency whose airfoil designs are commonly used in modern aerodynamics.
Reynolds number, Re	Dimensionless quantity used to characterize a fluid. It is the ratio of momentum forces to viscous forces and is used to determine similarity between two fluids.
Stall	A reduction in lift and increase in drag generated by a lifting body, usually due to an increase in angle of attack.
Vorticity, ω	The curl of a velocity field, describing the local spinning motion near a point in a fluid.
Wake age, ζ	The time elapsed since the creation of a trailing vortex, expressed in terms of the angular displacement (degrees of rotation) of the corresponding blade.

Bibliography

[1] Fish, F. E., and Battle, J. M. Hydrodynamic Design of the Humpback Whale Flipper. *Journal of Morphology*, 225(1):51–60, 1995.

[2] Miklosovic, D. S., Murray, M. M., Howle, L. E., and Fish, F. E. Leading-Edge Protuberances Delay Stall on Humpback Whale (Megaptera novaeangliae) Flippers. *Physics of Fluids*, 16(5):39–42, 2004.

[3] Bai, C. J., Lin, Y. Y., Lin, S. Y., and Wang, W. C. Computational Fluid Dynamics Analy- sis of the Vertical Axis Wind Turbine Blade with Protuberance Leading-Edge. *Journal of Renewable and Sustainable Energy*, 7(3):033124, 2015.

[4] Zhang, R. K., Wu, J. Z., and Chen, S. Y. A New Active Control Strategy for Wind-Turbine Blades under Off-Design Conditions. *International Journal of Modern Physics*, 19:283–292, 2012.

[5] Bolzon, M. D., Kelson, R. M., and Arjomandi, M. Tubercles and Their Applications. *Journal of Aerospace Engineering*, 29(1):04015013, 2015.

[6] CFD Analysis of Novel Biomimetically Inspired Helicopter Rotor Geometries. Technical Report 0117059, Sikorsky Aircraft Corp., October 2011.

[7] Leishman, J. G. *Principles of Helicopter Aerodynamics*. Cambridge University Press, New York, NY, 2006.

[8] Barbarino, S., Bilgen, O., Ajaj, R. M., Friswell, M. I., and Inman, D. J. A Review of Morph- ing Aircraft. *Journal of Intelligent Material Systems and Structures*, 22(9):823–877, 2011.

[9] Pedro, H. T. C., and Kobayashi, M. H. Numerical Study of stall Delay on Humpback Whale Flipper. In *Paper AIAA-90-3008, Proceedings of the 46th AIAA Aerospace Sciences Meeting and Exhibit*, Reno, NV, January 7–10, 2008.

[10] Hansen, K. L., Kelso, R. M., and Dally, B. B. Performance Variations of Leading-Edge Protuberances for Distinct Airfoil Profiles. *AIAA Journal*, 49(1):185–194, 2011.

[11] Hansen, K. L. Effect of Leading-Edge Tubercles on Airfoil Performance. Ph.d. dissertation, Department of Mechanical Engineering, University of Adelaide, Adelaide, Australia, 2012.

[12] Mai, H., Dietz, G., Geiler, W., Richter, K., Bosbach, J., Hugues, R., and de Groot, K. Dynamic Stall Control by Leading-Edge Vortex Generators. *Journal of the American Helicopter Society*, 53(1):26–36, 2008.

[13] Heine, B., Mulleners, K., Joubert, G., Raffel, M. Dynamic Stall Control by Passive Disturbance Generators. *AIAA Journal*, 51(9):2086–2097, 2013.

[14] Johari, H., Henoch, C., Custodio, D., and Levshin, A. Effects of Leading-Edge Protuberances on Airfoil Performance. *AIAA Journal*, 45(11):2634–2642, 2007.

[15] van Nierop, E. A., Alben, S., and Brenner, M. P. How Bumps on Whale Flippers Delay Stall: an Aerodynamic Model. *Physical Review Letters*, 100(5):054502, 2007.

[16] Miklosovic, D. S., Murray, M. M., and Howle, L. E. Experimental Evaluation of Sinusoidal Leading-Edges. *Journal of Aircraft*, 44(4):1404–1407, 2007.

[17] Stein, B., and Murray, M. M. Stall Mechanism Analysis of Humpback Whale Flipper Models. In *Paper AIAA-90-3008, Proceedings of Unmanned Untethered Submersible Technology (UUST)*, January, 2005.

[18] Fish, F. E., Weber, P. W., Murray, M. M., and Howle, L. E. The Tubercles on Humpback Whales Flippers: Application of Bio-Inspired Technology. *Integrative and Comparative Biology*, 51(1):203–213, 2011.

[19] Murray, M. M. Effects of Leading-Edge Protuberances on a Representative Whale Flipper Model at Various Sweep Angles. In *Proceedings of the 14th International Symposium on Unmanned Untethered Submersible Technology*, Durham, NH, August, 2005.

[20] Zhang, R. K., and Wu, J. Z. Aerodynamic Characteristics of Wind Turbine Blades with a Sinusoidal Leading-Edge. *Wind Energy*, 15(3):407–424, 2012.

[21] Gruber, T., Murray, M. M., and Fredriksson, D. W. Effect of Humpback Whale Inspired Protuberances on Marine Tidal Turbine Blades. In *ASME 2011 International Mechanical Engineering Congress and Exposition*, pages 851–857. American Society of Mechanical Engineers, 2011.

[22] Dropkin, A., Custodio, D., Henoch, C. W., and Johari, H. Computation of Flowfield Around an Airfoil with Leading-Edge Protuberances. *Journal of Aircraft*, 49(5):1345–1355, 2012.

[23] Leishman, J. G. On Seed Particle Dynamics in Tip Vortex Flows. *Journal of Aircraft*, 33(4):823–825, 1996.

[24] Prasad, A. J. Particle Image Velocimetry. *Current Science*, 79(1):51–60, 1997.

[25] Grant, I. Particle Image Velocimetry: a Review. *Institution of Mechanical Engineers*, 211(1):55–76, 1997.

[26] Anderson, J. D. *Fundamentals of Aerodynamics*. Mcgraw-Hill Companies Inc., New York, NY, 2005.

[27] Ramasamy, M., Johnson, B., and Leishman, J. G. Tip Vortex Measurements using Dual Plane Digital Particle Image Velocimetry. In *American Helicopter Society 64th Annual Forum Proceedings*, Montréal, Canada, April 29–May 1, 2008.

[28] Milluzzo, J., and Leishman, J. G. Fluid Dynamics of the Helicoidal Wake Sheets Trailed from a Hovering Rotor. *Journal of the American Helicopter Society*, 61(1):1–17, January 2016.

[29] Milluzzo, J., and Leishman, J. G. Vortical Sheet Behavior in the Wake of a Rotor in Ground Effect. *AIAA Journal*, 55(1):24–35, January 2017.

[30] Hall, P. Taylor–Görtler Vortices in Fully Developed Boundary Layer Flows. *Journal of Fluid Mechanics*, 124(3):475–494, 1982.

[31] Smith, D. E., and Sigl, D. Helicopter Rotor Tip Shapes for Reduced Blade-Vortex Interaction – An Experimental Investigation. In *AIAA Paper 95-0192, 33rd Aerospace Sciences Meeting and Exhibit*, Reno, NV, January 9–12, 1995.

[32] Mullins, B. R., Smith, D. E., Rath, C. B., Thomas, S. L. Helicopter Rotor Tip Shapes for Reduced Blade-Vortex Interaction – An Experimental Investigation II. In *AIAA Paper 96-0149, 34th Aerospace Sciences Meeting and Exhibit*, Reno, NV, January 15–18, 1996.

[33] Milluzzo, J. I. and Leishman, J. G. Assessment of Rotorcraft Brownout Severity in Terms of Rotor Design Parameters. *Journal of the American Helicopter Society*, 55(3):32009–32009, 2010.

[34] Milluzzo, J., and Leishman, J. G. Quantification of the Evolution of a Vortical Sheet in the Wake of a Hovering Rotor. In *44th AIAA Fluid Dynamics Conference*, Atlanta, GA, June 16–20, 2014.

[35] Takahashi, R. K. and McAlister, K. W. Preliminary Study of a Wing-Tip Vortex Using Laser Velocimetry. Technical Report 88,343, NASA TM, January 1987.

[36] Yamauchi, G. K., Burley, C. L., Mercker, E., Pengel, K., and Janakiram, R. Flow Measurements of an Isolated Model Tilt Rotor. In *Proceedings of the 55th Annual American Helicopter Society Forum*, Montreal, Canada, May 2527, 1999.

[37] Ramasamy, M., Johnson, B., Huismann, T., and Leishman, J. G. Digital Particle Image Velocimetry Measurements of Tip Vortex Characteristics Using an Improved Aperiodicity Correction. *Journal of the American Helicopter Society*, 54(1):1–13, 2009.

[38] Ramasamy, M., and Bhagwat, M. J. Effect of Tip Vortex Aperiodicity on Measurement Uncertainty. *Experiments in Fluids*, 53(5):11911202, July 2012.

[39] van der Wall, B. G., Burley, C. L., Yu, Y., Richard, H., Pengel, K., and Beaumierf, P. The HART II Test Measurement of Helicopter Rotor Wakes. *Aerospace Science and Technology*, 8(4):273–284, June 2004.

[40] van der Wall, B. G., and Richard, H. Analysis Methodology for 3C PIV Data of Rotary Wing Vortices. *Experiments in Fluids*, 40(5):798–812, May 2006.

[41] van der Wall, B. G., and Schneider, O. Conditional Averaging Methodology for Periodic Data with Time Jitter and Spatial Scatter. In *Proceedings of the 33rd European Rotorcraft Forum*, Kazan, Russia, September 11-13, 2007.

[42] Duraisamy, K. Ramasamy, M., Baeder, J. D., and Leishman, J. G. High-Resolution Computational and Experimental Study of Rotary-Wing Tip Vortex Formation. *AIAA Journal*, 45(11):2593–2602, November 2007.